Distributed sensing of microseisms and teleseisms with submarine dark fibers

Ethan F. Williams[1,2], Maria R. Fernández-Ruiz[3], Regina Magalhaes[3], Roel Vanthillo[4], Zhongwen Zhan[2], Miguel González-Herráez[3], Hugo F. Martins[5]

Manuscript accepted in *Nature Communications*

October 21, 2019

Abstract

Sparse seismic instrumentation in the oceans limits our understanding of deep Earth dynamics and submarine earthquakes. Distributed acoustic sensing (DAS), an emerging technology that converts optical fiber to seismic sensors, allows us to leverage pre-existing submarine telecommunication cables for seismic monitoring. Here we report observations of microseism, local surface gravity waves, and a teleseismic earthquake along a 4192-sensor ocean-bottom DAS array offshore Belgium. We observe in-situ how opposing groups of ocean surface gravity waves generate double-frequency seismic Scholte waves, as described by the Longuet-Higgins theory of microseism generation. We also extract P- and S-wave phases from the 2018-08-19 M_w8.2 Fiji deep earthquake in the 0.01-1 Hz frequency band, though waveform fidelity is low at high frequencies. These results suggest significant potential of DAS in next-generation submarine seismic networks.

Introduction

One of the greatest outstanding challenges in seismology is the sparsity of instrumentation across Earth's oceans [1, 2]. Poor spatial coverage results in biases and low-resolution regions in global tomography models as well as significant location uncertainty for offshore seismicity. Modern ocean-bottom seismometers (OBS) generally fall into two categories: short-period instruments (∼1-5 Hz), which can

[1] Corresponding Author: efwillia@gps.caltech.edu
[2] Seismological Laboratory, California Institute of Technology, 1200 E. California Blvd., Pasadena, CA 91125-2100, USA
[3] Department of Electronics, University of Alcalá, Polytechnic School, Alcalá de Henares, Madrid 28871, Spain
[4] Marlinks, Sint-Maartenstraat 5, 3000 Leuven, Belgium
[5] Instituto de Óptica, CSIC, 28006 Madrid, Spain

record for up to a month or more, and long-period or broadband instruments (BBOBS), which often employ the same sensors as terrestrial broadband seismic stations and can operate for as long as two years [3]. Whereas short-period instruments are primarily used in active-source experiments, BBOBS are ideal for passive-source experiments and have been used for tomographic studies, earthquake location, and ocean wave monitoring among numerous other applications [4–12]. However, BBOBS are expensive and limited by data telemetry and battery life except in near-shore environments [3]. Recent work has explored several alternatives to conventional BBOBS for offshore seismic monitoring, including free-floating robots equipped with hydrophones [13], moored surface buoys or autonomous surface vehicles for satellite telemetry acoustically linked to BBOBS [14, 15], and cabled arrays of broadband sensors [16]. Recently, Marra et al. [17] applied laser interferometry to convert long ocean-bottom telecommunications optical fiber links into seismic strainmeters. This work is particularly promising because repurposing the >1 million km of pre-existing trans-oceanic telecommunications cables as seismic sensors would permit rapid detection and location of earthquakes throughout the world's ocean basins. Unfortunately, the particular technique in Marra et al. [17] is limited to measuring propagation delays integrated across an entire cable length, resulting in a single seismograph with equivalent station location uncertainty on the order of 1 km and complicated instrument response.

Distributed acoustic sensing (DAS) is an emerging technology with strong potential to form the core of next-generation submarine seismic monitoring infrastructure. A DAS interrogator unit probes a fiber-optic cable with a coherent laser pulse and measures changes in the phase of the returning optical backscatter time-series. Optical phase shifts between pulses are proportional to longitudinal strain in the fiber and can be mapped into the finite, distributed strain across a fiber segment (termed gauge length) by integration. Applying DAS technology to a fiber-optic cable effectively converts the cable into a seismic recording array with thousands of single-component channels, real-time data telemetry, and unlimited deployment duration as long as the DAS unit is powered. For about a decade, DAS has been successfully utilized in boreholes for active-source seismic profiling [18–20]. Recent work with onshore trenched or conduit-installed horizontal fibers has demonstrated the ability of DAS arrays to record earthquakes and other seismic signals at local to teleseismic distances with high waveform fidelity [21–28].

In this paper, we demonstrate that submarine horizontal DAS arrays utilizing pre-existing ocean-bottom fiber-optic cables are similarly effective for seismological studies and can also record pressure perturbations from ocean wave phenomena. We first examine ocean surface gravity waves and associated seismic modes directly observed on an ocean-bottom DAS array offshore Zeebrugge, Belgium, which we interpret as evidence of in-situ microseism generation. We then report our observation of body waves from the 2018-08-19 $M_w8.2$ Fiji deep earthquake. Finally, we discuss implications for future DAS deployments in marine settings.

Results

Experiment Overview

The Belgium DAS array (BDASA) occupied a pre-existing ocean-bottom fiber-optic cable in the Southern Bight of the North Sea offshore Zeebrugge, Belgium (Fig. 1). During August of 2018, the BDASA recorded continuously for nearly a month. Here, we analyze the 1-hr record containing the principal body wave phases from the 2018-08-19 M_w8.2 Fiji deep earthquake, along with ocean wave signals and microseism noise. The fiber-optic cable was originally installed to monitor a power cable for the Belwind Offshore Wind Farm (cable and fiber specifications are given in the Supplementary Note 1, Supplementary Figure 1). Cable geometry is approximately straight over four 10-km segments and is flat or shallowly dipping, except for a steep channel around 10 km and two ∼15 m bathymetric ridges at ∼30 and 40 km from the coast (Fig. 1A). The cable is buried between 0.5 and 3.5 m below the seafloor in water depths shallower than 40 m. A chirped-pulse DAS system built and installed by the University of Alcala [29] continuously interrogated a 42-km near-shore segment of the fiber with channel spacing of 10 m, creating 4192 simultaneously recording seismic sensors (see Methods).

In Separation of Coherent Signals, we first decompose the raw BDASA data in the frequency-wavenumber domain, separating and identifying oceanic and seismic signals. In Microseism Generation, we compare our observations of ocean surface gravity and Scholte waves to the Longuet-Higgins [30] theory of double-frequency microseism generation. In Ocean Waves and Ocean Currents, we describe sea state and ocean currents across the BDASA, evident from variations in the symmetry of ocean surface gravity wave dispersion. Finally, we discuss the quality of teleseismic body waves from 2018-08-19 M_w8.2 Fiji deep earthquake, recovered from the BDASA after filtering out ocean wave and microseism signals.

Separation of Coherent Signals

In the time-domain, raw strain records from the BDASA are complicated by the superposition of several coherent signals with incoherent noise from sources such as temperature drift (Fig. 2A). In the frequency-domain, the power spectral density (PSD) of each channel exhibits five distinct peaks, corresponding to different wave modes propagating across the array (Fig. 2B). In order to identify and interpret the wave types comprising each peak, we apply a 2D Fast Fourier Transform from the raw strain records into the frequency-wavenumber (f-k) domain (Fig. 3). F-k domain analysis of the raw BDASA data is possible here because the chirped-pulse DAS system exhibits negligible fading of sensitivity along the fiber, as is common in conventional DAS and which would require pre-processing at the expense of bandwidth (see Methods). Given the quasi-linear geometry of the fiber cable, no corrective algorithms or fiber sectioning methods were applied to compensate cable turns, resulting in slight smearing of energy along the wavenumber axis.

Visualization of BDASA data in the f-k domain allows identification and separation of coherent seismic and oceanic signals in each frequency band based on their characteristic phase velocities ($c = f/k$). Figure 3A shows the complete 4192-channel, 1-hr dataset transformed into a single f-k spectrum. Energy in quadrants 1 and 3 corresponds to waves with positive phase velocities. In the coordinate system we adopted, this represents waves propagating landward across the array. Similarly, energy in quadrants 2 and 4 corresponds to waves with negative phase velocities, propagating seaward across the array. There are two distinct groups of energy in the f-k spectrum, which are easily visualized in log-log space (Fig. 3B). Ocean waves appear at low frequencies (<0.3 Hz) with apparent phase velocity slower than ∼17 m/s. Seismic waves appear at high frequencies (>0.3 Hz) with apparent phase velocity faster than ∼300 m/s. Teleseismic body waves from the M_w8.2 Fiji deep earthquake are not directly visible in the f-k spectrum.

Ocean Surface Gravity Waves

Surface gravity and infragravity waves are excited in oceanic waters by wind-sea interaction. Ocean surface gravity waves follow the dispersion relation $\omega^2 = gk\tanh(kH)$, where ω is angular frequency, g is gravitational acceleration, k is angular wavenumber, and H is water depth (e.g. [31]). F-k analysis of BDASA data shows strong, coherent energy packets in all four quadrants between <0.01 and 0.3 Hz (Fig 4A) with peaks at 0.09 and 0.18 Hz (Fig. 2B). The upper edge of these packets follows the ocean surface gravity wave dispersion relation, corresponding to energy propagating axially along the cable both landward and seaward. Energy appearing below this edge represents surface gravity waves with faster apparent phase velocity that obey the same dispersion relation but are obliquely incident to the cable. For the 20-30 km cable segment shown in Figure 4A, landward-propagating ocean surface gravity waves are stronger than seaward-propagating waves.

We project the f-k spectrum into frequency-phase velocity space (f-c) using the coordinate transformation $c = f/k$, permitting better visualization of phase velocity dispersion (Fig. 4B). In f-c space, ocean surface gravity waves exhibit coherent dispersion from faster phase velocity ($\sim$ 17 m/s) at low frequencies ($\sim$ 0.01 Hz) to slower phase velocity ($\sim$ 6 m/s) at 0.3 Hz. Ocean wave energy tapers off quickly above 0.3 Hz.

Scholte (Seismic) Waves

Seismic waves propagating faster than 300 m/s are represented in the f-k domain by symmetric fans of energy at frequencies >0.3 Hz (Fig. 5A) with peaks at 0.36 and 1.12 Hz (Fig. 2B). When projected from the f-k domain into f-c space, the high-frequency energy packet exhibits strong dispersion from phase velocities close to the compressional velocity of water (∼1500 m/s) at 0.36 Hz to an asymptotic velocity of ∼300 m/s above 1 Hz (Fig. 5B). This is consistent with the expected dispersion relation of Scholte waves along the sediment-water interface, which follows the compressional velocity of water at low frequencies and the shear-wave velocity of the shallow sediment layer at high frequencies [32]. As for ocean waves, the low-velocity edge of the f-k energy packets in each quadrant represents Scholte waves propagating axially along the cable. Energy appearing at faster apparent phase velocities represents Scholte waves obliquely incident to the cable. We note that the 0.3-3.5 Hz Scholte waves are observed in the 550 s of data preceding the arrival of the first P-wave phases from the Fiji earthquake and therefore must be an independent, local phenomenon.

Microseism Generation

Globally, seismograms record broadband seismic noise with peaks around 14 and 7 s period, termed microseisms, which have long been attributed to ocean wave sources (e.g. [33]). The longer period (lower frequency) peak is commonly referred to as primary microseism, while the shorter period (higher frequency) peak is called secondary microseism. Source locations of primary microseism appear to be restricted to coastal areas, with seismic noise excited by direct loading of the seafloor where gravity waves impinge on shallow coastal waters [34, 35]. Source locations of secondary microseism, however, include both near-shore and deep-water environments [35, 36], and the amplitude of the secondary microseism peak has not been tied directly to coastal ocean wave conditions (e.g. [37]). While the relative amplitude and central frequencies of the microseism peaks vary by region and sea state, the double-frequency relationship between primary and secondary microseism is universal and a subject of continued research. Here, we argue that ocean surface gravity waves and Scholte waves observed on the BDASA at double-frequency (0.18 and 0.36 Hz respectively) together represent in-situ microseism generation following the theory of Longuet-Higgins [30].

Primary Microseism and its Depth Dependence

Based on our f-k analysis above, the 0.18 Hz peak in Figure 2B corresponds to ocean surface gravity waves propagating across the BDASA. Because the cable is buried at a depth of 0.5-3.5 m, the BDASA is only mechanically coupled to the water body above through the intermediary shallow sediment layer, so ocean waves cannot be observed directly. Instead, ocean waves signals observed on the BDASA are poroelastic strains in the solid earth induced by the pressure field of ocean waves propagating above, hence primary microseism generated in-situ by ocean wave loading. Common observations of primary microseism on terrestrial seismic networks (e.g. [35]) constitute diffuse seismic energy radiated into the far-field, whereas here we observe the primary microseim source directly.

To test this interpretation, we compare the variation in amplitude of the 0.18 Hz peak to the expected seafloor pressure under ocean surface gravity waves along the cable depth profile. The strength of ocean surface gravity waves decays rapidly with depth, which is why source regions of primary microseism are constrained to the coast. Invoking linear wave theory, the magnitude of the pressure perturbations at the seafloor beneath a surface gravity wave scales with angular wavenumber k and water depth H as $p_d \propto \mathrm{sech}(kH)$ (e.g. [31]). To evaluate p_d, we iteratively solve the implicit dispersion relation for ocean surface gravity waves, $\omega^2 = gk\tanh(kH)$, to obtain $\omega(k)$, and then calculate a theoretical p_d as a function of distance and depth using the cable profile. In order to determine a scaling factor between seafloor pressure and fiber strain, we fit the Fourier amplitude observed on the BDASA at 0.18 Hz as a linear function of theoretical p_d (see Supplementary Note 2), to produce the model plotted in Figure 6. We observe a good correspondence between the observed and modeled Fourier amplitude at 0.18 Hz with both water depth and distance along the cable (Fig. 6). To leading order, then, 0.18 Hz energy observed on the BDASA is proportional to pressure applied by ocean surface gravity waves at the seafloor, confirming our interpretation of primary microseism generation.

Secondary Microseism by Ocean Wave Interaction

Longuet-Higgins [30] first proposed a mechanism for the double-frequency nature of microseisms, whereby nonlinear interaction of opposing groups of surface gravity waves at one frequency generates a depth-invariant pressure term of second-order magnitude which oscillates at twice the frequency of the surface waves. Hasselmann [38] expanded this theory to demonstrate that appreciable microseisms are excited only by components of the ocean pressure field that match the phase velocities of the seismic modes of the coupled water-seabed system. In the simplest case, the phase velocity of Longuet-Higgins's second-order pressure term scales as $c = 2\omega/\|\vec{k}_1 + \vec{k}_2\|$ for two plane surface gravity waves with phase $\vec{k}_1 \cdot \vec{x} - \omega t$ and $\vec{k}_2 \cdot \vec{x} - \omega t$. Hence, for opposing waves (when $\vec{k}_1$ is close to $-\vec{k}_2$), c approaches seismic velocities.

Based on these theories, we assert that the 0.36 Hz Scholte waves discussed above represent secondary microseism associated with the 0.18 Hz opposing surface gravity wave groups. Unlike the 0.18 Hz energy peak, the 0.36 Hz peak observed in the BDASA PSD is almost invariant with depth and is not adequately described by the pressure-depth scaling of ocean surface gravity waves (Fig. 6A). Instead, the Fourier amplitude at 0.36 Hz decreases over the first 12-15 km of the array and then increases gradually with distance out to 40 km (Fig. 6B). Therefore, Scholte waves at 0.36 Hz cannot be the product of direct loading by ocean surface gravity waves.

Longuet-Higgins [30] predicts that the amplitude of the secondary pressure term generated by non-linear wave interaction is proportional to the product of the amplitudes of the two opposing ocean wavefield components. Hence, we expect to observe the strongest Scholte waves where seaward- and landward-propagating ocean surface gravity waves are of similar strength and the weakest Scholte waves where seaward- and landward-propagating ocean waves are of significantly different strengths. To test this property, we plot directional spectra for both ocean surface gravity waves and Scholte waves (Fig. 7). For each wave type, theoretical dispersion curves are constructed for waves with different incident azimuths. For each of four 10-km quasi-linear segments along the fiber, we then take the mean f-k spectral amplitude interpolated along each dispersion curve to form the polar plots in Figure 7 (see Supplementary Note 3). The cable segment in water depths < 10 m is neglected in this analysis, as the PSD of this region is saturated by incoherent energy across a broad band, likely associated with shoaling of ocean waves.

The relative strength of seaward- and landward-propagating ocean surface gravity wavefield components is most similar for the 30-40 km segment, slightly less equal for the 10-20 km segment, and most disparate for the 20-30 km segment (Fig. 7A). As predicted by this scaling, the absolute strength of the Scholte wavefield components (in both quadrants) is greatest for the 30-40 km segment, less for the 10-20 km segment, and smallest for the 20-30 km segment (Fig. 7B). Note that because Longuet-Higgins's second-order pressure term does not decay with depth, this result is dependent only on the relative strengths of ocean wavefield components shown in Figure 7A, and not their absolute strength.

For Scholte (similar to Rayleigh) waves, the theoretical azimuthal sensitivity of DAS is approximately $cos^2(\theta)$, where $\theta = 0$ is along the axis of the fiber, in the limit that the wavelength is much longer than the gauge length used by the DAS system [39]. The directional spectra shown in Figure 8B all approximately follow a cos^2 shape, suggesting that the azimuthal distribution of Scholte wave energy is relatively diffuse (or isotropically propagating) along most of the fiber. The diffuse nature of the secondary microseism wavefield is further evidence that these waves must be generated in-situ and also offers a direct observation of the radiation pattern of secondary microseism at its source.

Within this framework, we are unable to describe the 1.12 Hz peak (Fig. 2B) and associated high-frequency Scholte wave energy observed up to 3.5 Hz (Fig. 5A). The 1.12 Hz peak likely does not represent secondary microseism associated with a pair of opposing surface gravity wave groups with dominant frequency of 0.55 Hz, as no 0.55 Hz peak is observed in our data. However, the strength of ocean waves observed at the seafloor attenuates strongly with decreasing wavelength, so it is possible that 0.55 Hz ocean waves do exist. The 1.12 Hz peak could also correspond to external environmental noise from an unknown (potentially anthropogenic) source. Alternatively, it could represent a resonant mode of the coupled sediment-water system.

Ocean Waves and Ocean Currents

Beyond their implications for microseism generation, ocean surface gravity waves observed on the BDASA demonstrate the potential of ocean-bottom DAS for investigations in physical oceanography. Computing f-k spectra across different segments of the cable, we can distinguish spatial variations in the intensity of landward-propagating versus seaward-propagating ocean surface gravity waves in order to interpret sea state. For example, on the 20-30 km segment (Fig. 4A) landward-propagating waves are stronger than seaward-propagating waves, while on the 30-40 km segment (Fig. 8A) landward-propagating and seaward-propagating waves are of similar strength (see also Fig. 7A). Because the strength of seaward-propagating waves is greater on the outermost segment of the cable than on the next segment closer to shore, we infer that some of the seaward-propagating waves must be local reflections from the bathymetric ridge at 30 km. Inboard of the 30-km ridge, we observe the ratio of seaward-propagating to landward-propagating wave energy decrease systematically, which is consistent with the expectation that all seaward-propagating ocean waves observed on the BDASA are generated by reflection from the sloping seabed approaching the coast. While the extent of our interpretation is limited by the 1-hr record length of BDASA data, the framework for ocean wave analysis demonstrated here would be easily applicable to monitor temporal variations in sea state over tidal to annual scales.

Because of the large number of channels and high-sample rate on the BDASA, f-k domain resolution is sufficiently fine to distinguish small perturbations in surface gravity wave dispersion associated with ocean currents. For example, the f-k spectrum of the last 10 km segment (30-40 km) is asymmetrical and evolves over the 1-hr record (only the last 10-minute window is shown in Fig. 8). On this segment, landward-propagating waves appear faster than sea-ward propagating waves, as the result of an ocean current with a component of flow in the landward direction along the array (Fig. 8B,C). We fit the dispersion asymmetry with a mean-flow correction to the dispersion relation $(\omega - Uk)^2 = gk\tanh(kH)$, which describes the first-order effect of surface gravity waves propagating in a current, where U is the apparent velocity of the current along the cable (as above, ω is angular frequency, k is angular wavenumber, g is gravitational acceleration, and H is water depth). Over the 1-hr record, the strength of the observed current increases gradually from 0.1 to 0.5 m/s apparent velocity in the landward direction. Contemporary methods of ocean current measurement are largely limited to either high-frequency radio observation of surface currents [40, 41] or in-situ observation of current-depth profiles using spatially-sparse moorings, drifters, or ship-board instruments [42–44]). Our observation of spatio-temporal variations in current speed is significant because it suggests potential application of ocean-bottom DAS to in-situ measurement and monitoring of ocean currents by exploiting models of wave interaction with heterogeneous currents (e.g. [45]) to recover high-resolution spatial variations in current speed along an array.

2018-08-19 $M_w8.2$ Fiji Deep Earthquake

Rapid, accurate measurement of body wave travel-times is an essential goal of next-generation broadband marine seismology [1] and has motivated many recent advances in ocean-bottom seismic instrumentation (e.g. [13]). Ocean-bottom DAS arrays are an ideal technological solution because they offer real-time telemetry and are intrinsically synchronized (all channels are interrogated with the same unit, thus avoiding any differential clock drift across the array), neither of which are easily achievable features of OBS networks. Northern Europe is a seismically quiescent area, so no local or regional seismic events were recorded. However, the BDASA captured teleseismic body waves from a $M_w8.2$ deep earthquake in the Fiji-Tonga area on August 19, 2018 (Fig. 1B). Teleseisms arrived from an epicentral distance of 146.7^o (>16,300 km), at a back azimuth of 358.5^o (27.6^o oblique to the mean fiber azimuth of 330.9^o). Because the 2018-08-19 Fiji event occurred at a depth of 600 km, only weak surface waves were excited and hence could not be analyzed.

Teleseismic body waves from the Fiji earthquake are close to vertically incident and expected to arrive almost simultaneously along the array, hence appearing at wavenumbers lower than can be resolved across a few kilometers aperture. In order to isolate teleseisms from ocean surface gravity and Scholte waves, we apply a 2D band-pass filter in the f-k domain between 0.001-1 Hz and 0-0.002 m^{-1} in the first and third quadrants (corresponding to energy propagating landward across the array from the north/west; Supplementary Figure 2), stack waveforms across a 5-km array segment to form a beam trace, and finally apply a range of bandpass filters to the beam trace to produce the BDASA waveforms shown in Figure 9 (see Supplementary Note 4). We compare the BDASA beam trace to nearby broadband seismometer BOST (30-50 km south of BDASA), after rotating the horizontal channels into the mean azimuth of the BDASA and bandpass filtering.

At high frequencies (>0.1 Hz), we recover the PKP phase ($\sim$550 s) and its associated pPKP + sPKP depth phases ($\sim$690 s), the travel times of which correspond well to those recorded on BOST (Fig. 9). The envelopes of the recovered P phases (not shown) are similar to those from BOST, although the they show low-to-moderate waveform fidelity (mean correlation coefficient of 0.25; Supplementary Figure 3, Supplementary Note 4). Hence, the polarity of the first P-wave arrival recovered from the BDASA is not reliable across parts of the array. Spatially variable P waveforms may be physical, however, as high frequency waves can be strongly affected by near-surface structures and the water layer. At low frequencies (<0.15 Hz), the background noise is substantially stronger, but we still recover a complex S wavetrain, which exhibits moderate-to-high waveform fidelity when compared with BOST (mean correlation coefficient of 0.6; Supplementary Figure 4). Recovered P and S waveforms are both coherent along the length of the array (Supplementary Figure 5).

Because the BDASA measures strain across a 10-m gauge length whereas BOST measures particle velocity at a single point, theoretical amplitudes are approximately proportional by a factor of the apparent horizontal slowness for wavelengths longer than twice the gauge length [26]. For the Fiji earthquake, the ratio of BDASA strain amplitude to BOST particle velocity amplitude does not yield reasonable apparent velocities for the observed phases across any band. Hence, we infer that strain-transfer coupling between the solid earth and the BDASA fiber, a consequence of the fiber casing and installation, is complex (see Supplementary Note 1, Supplementary Figure 1).

While a $M_w8.2$ deep earthquake is a rare and particularly large event, body wave energy observed in Belgium at 146.7^o epicentral distance is lower in spectral amplitude than would be expected for regional earthquakes ($< 1^o$ epicentral distance) greater than $\sim M3.5$ (see Supplementary Note 6; Supplementary Figure 6). Hence, BDASA clearly exhibits teleseismic and regional seismic monitoring capability, as both P-wave and S-wave travel-times can be recovered across a broad band, and S-wave polarity is robust over the frequencies of interest to global seismology.

Discussion

We have presented and analyzed our observations of seismic and ocean waves on an ocean-bottom DAS array offshore Belgium, demonstrating that DAS arrays utilizing existing ocean-bottom fiber optic installations can offer high value seismographic and oceanographic data products. In particular, we recovered both P- and S-phases from the 2018-08-19 Fiji deep earthquake, though only S-waves exhibited moderate-to-high waveform fidelity. While we were unable to recover robust polarity of high-frequency P-phases, we can expect that ocean-bottom DAS arrays in deep water would have much lower detection thresholds for seismic signals than observed here, as has been demonstrated for OBS (e.g. [46]). For an ocean-bottom DAS array, the noise floor can be considered as the superposition of instrumental noise from the DAS interrogator unit and fiber, temperature noise from variations in pore fluid temperature, pressure noise from ocean waves, and seismic noise. The aggressive filtering procedure we applied to recover teleseismic waveforms was necessitated to remove environmental signal, not instrument noise, as coherent signals of physical origin were observed across the full band of interest (0.01-5 Hz). Onshore studies with DAS arrays have found that instrument noise is approximately inversely proportional to frequency with a noise floor no higher than 1 $\mu\varepsilon/\mathrm{Hz}^{1/2}$ at 1 Hz [47]. Laboratory experiments show that in a stable temperature environment, DAS systems can exhibit a noise floor below 100 p$\varepsilon/\mathrm{Hz}^{1/2}$ at 1 Hz [48]. On a DAS array, a temperature perturbation of 1 mK is indistinguishable from a 10 nε strain, so high-frequency temperature fluctuations along the fiber can contribute spurious signals. Water-bottom temperatures may vary on the order of 1 K at tidal periods in the near-shore environment; however, such variability attenuates strongly with depth and is inversely correlated to frequency (e.g. [49, 50]). Consequently, instrumental and temperature noise are not limiting factors for most seismological applications, as seen here. In deep water settings, the magnitude of pressure oscillations beneath ocean surface gravity waves, the primary environmental noise which dominates BDASA data between 0.01 and 0.26 Hz, decays exponentially with depth. Therefore, the shallow-water setting of the BDASA actually represents a 'worst case' environment for recording teleseismic events [46, 51], and thus our ability to recover both P- and S-phases is particularly significant.

Compared to traditional OBS deployments, another advantage of DAS is the number and density of stations. Utilizing hundreds of stations from any segment of the array we were able to apply array-based processing in order to distinguish seismic and ocean signals based on their phase information. So-called "large N" deployments permit low detection thresholds for small earthquakes, precise location of earthquakes, low uncertainty in travel-time measurements, and high-resolution imaging studies [25, 52, 53]. Further, we have demonstrated that large-N ocean-bottom networks open up new possibilities in studying ocean wave phenomena and microseism generation. The vast majority of studies examining the physics of ocean microseism generation have been limited to remote observation of radiated energy on terrestrial broadband networks [33, 37, 54, 55]. The few studies utilizing ocean-bottom instrumentation to correlate ocean-wave phenomena with microseism in-situ have been restricted by small network size, effectively resulting in measurements of microseism direction and intensity at a single point with or without simultaneous ocean wave information, and have had mixed success in validating theoretical models [36, 56–60]. Simultaneous observation of ocean pressure variations and seismic noise across several thousand channels on ocean-bottom DAS arrays of arbitrary geometry permits reconstruction of the full surface gravity wave and Scholte wave fields, as shown here, and, with the addition of a time-lapse component to future surveys, offers a leap forward in our ability to study microseism and its source processes.

However, several technological challenges still remain before DAS systems can complement or even replace BBOBS on a global scale. Foremost is the axial (single-component) directional sensitivity of DAS. Though work with helically wound optical fibers offering multi-component DAS sensitivity is underway [61], modern BBOBS already provide four-component (three-component + pressure) recording capability with the same state-of-the-art instruments used in terrestrial networks. We noted that teleseismic waveforms recovered from the BDASA did not exhibit coherent strain amplitude when compared with particle velocity at BOST, suggesting that the mechanics of strain transfer from the solid earth across the cable housing and into the optical fiber are complex and deserve further study [62]. In the laboratory, DAS exhibits a linear frequency response, resulting in correct amplitude and distortion free waves [24, 28, 63], hence amplitude preservation may be currently limited by installation conditions and not by the DAS technology itself. Finally, ocean-bottom DAS deployments are not presently possible in remote oceanic locations. Most commercial DAS systems and laboratory measurements claim operation across up to 50 km of fiber, with sensitivity decreasing along the fiber due to optical attenuation. With the use of more complex pulse formats or distributed amplification, the sensing range can be extended to 70-100 km [64–66] with a more even distribution of sensitivity along the fiber, while still using a standard telecom fiber installation. In principle, longer distances can be achieved with complex dedicated fiber installations and power supply along the fiber link (via use of optical repeaters [67, 68] and/or multiple stage distributed amplification [65, 69]), but the impact on the cost and DAS sensitivity means that such systems are not currently practical.

Methods

Chirped-pulse Distributed Acoustic Sensing

A chirped-pulse DAS [29] was used for the interrogator system, assisted by first order co-propagating Raman amplification [66]. In comparison with conventional DAS systems, chirped-pulse DAS offers high signal-to-noise ratio (SNR) and low variations in sensitivity along the fiber [48, 66, 70]. The key of its performance lies in the use of a linearly chirped probe pulse for the time-domain interrogation. Temperature or strain perturbations around the fiber affect its refractive index, which in turn slightly alters the central wavelength of the propagating light. An appropriately high linear chirp in the probe pulse (i.e., that inducing a spectral content much higher than the spectral content of the transform limited pulse) induces a local wavelength-to-time mapping arising from the temporal far-field condition [71]. Hence, variations in the central wavelength of the propagating light translate into temporal shifts in the trace at the particular location of the perturbation. The perturbation is then quantified by a time-delay estimation process via local trace-to-trace correlations over temporal windows similar to the probe pulse width.

The principle of operation of chirped-pulse DAS substantially improves the performance of the sensor over conventional DAS schemes. First, strain perturbations can be properly quantified by simply using direct detection. This contrasts with the conventional case, in which it is necessary to detect the trace optical phase for that purpose. Avoiding phase detection brings important advantages. Coherent detection imposes stringent requirement in the coherence length of the laser source, as it limits the DAS operation range due to the need for beating with a local oscillator. In chirped-pulse DAS, the coherence length of the probe laser can be relaxed, in principle simply requiring it to be substantially higher than the pulse width, with almost no detrimental effect on the acoustic SNR [72]. Polarization fading is not observed in chirped-pulse DAS (due to use of direct detection). More importantly, sensitivity of conventional DAS completely fades in certain points along the fiber (acoustic SNR <1 in up to 6% of fiber locations considering a healthy-SNR optical trace) due to the impossibility of maintaining the phase reference in low intensity trace regions caused by its interferometric nature [73]. Those blind spots need to be corrected using complex post-processing techniques or multi-wavelength measurements [74], typically at the expense of sensing bandwidth and higher measurements times. Chirped-pulse DAS, however, shows no fading sensitivity, enabling the raw strain signal as measured by the DAS to be directly processed without using any denoising/smoothing algorithm. This steady sensitivity is particularly beneficial for the subsequent 2D processing applied to isolate seismic events from other sources, since all points are captured with similar noise/sensitivity along the whole fiber length (>40 km) [70].

In addition, signal attenuation due to fibre loss is greatly mitigated in our scheme with the use of distributed Raman amplification. Note that in Pastor-Graells et al. [66], the fiber trace optical power fluctuation along a 75-km link is kept below 7 dB, as opposed to the $\sim$28.5 dB attenuation expected without distributed amplification (28.5 dB $=75\text{km}\times2\times0.19$ dB, using 0.19 dB/km as typical standard single mode fiber loss; note that roundtrip DAS attenuation is twice that of the fiber transmission losses). In this study, we observed DAS trace power fluctuations lower than 3 dB along the 42-km fiber. This is in contrast with the optical signal attenuation of $\sim$16 dB ($= 42\text{km}\times2\times0.19\text{dB/km}$) expected without distributed amplification.

The optical resolution (or gauge length) and channel spacing of the employed sensor were both 10 m (equivalent to one seismometer placed very 10 m, measuring distributed strain over a length of 10 m), totaling 4192 channels over 42 km. Each channel was sampled at 1 kHz and later downsampled to 10 Hz in order to reduce the dataset size.

Data Availability

Raw strain records from the BDASA are available on a public data repository at the following DOI: `http://dx.doi.org/10.22002/D1.1296`. More information about reading and processing data files can be obtained from the authors upon request.

Code Availability

All code required to reproduce the figures in this paper is written in Python and available from the authors upon request.

Acknowledgements

We thank Jörn Callies, Victor Tsai, and Andrew Thompson for insightful discussions. This work was supported in part by the members of the Space Innovation Council at Caltech, the Caltech-JPL President's and Director's Research and Development Fund (PDRDF), the DOMINO Water JPI project under the WaterWorks2014 cofounded call by EC Horizon 2020 and Spanish MINECO, and the regional program SINFOTON2-CM: P2018/NMT-4326. E.F.W. was supported by an NSF Graduate Research Fellowship. M.R.F.R. and H.F.M. acknowledge financial support from the Spanish Ministerio de Ciencia, Innovación y Universidades (CIENCIA) under contracts no. FJCI-2016-27881 and IJCI-2017-33856, respectively. R.M. acknowledges financial support from the EU's Horizon 2020 research and innovation program under the Marie Sklodowska-Curie Action grant agreement no. 722509EU (ITN-FINESSE). Z.Z. acknowledges support under NSF CAREER Award 1848166. M.G.H. acknowledges funding from the Spanish MINECO through projects TEC2015-71127-C2-2-R and RTI2018-097957-B-C31.

Author Contributions

E.F.W., M.R.F.R., and H.F.M. carried out data analysis and wrote the manuscript; R.M. and R.V. acquired the data; Z.Z. and M.G.H. advised data analysis and edited the manuscript.

Competing Interests

The authors declare no competing interests.

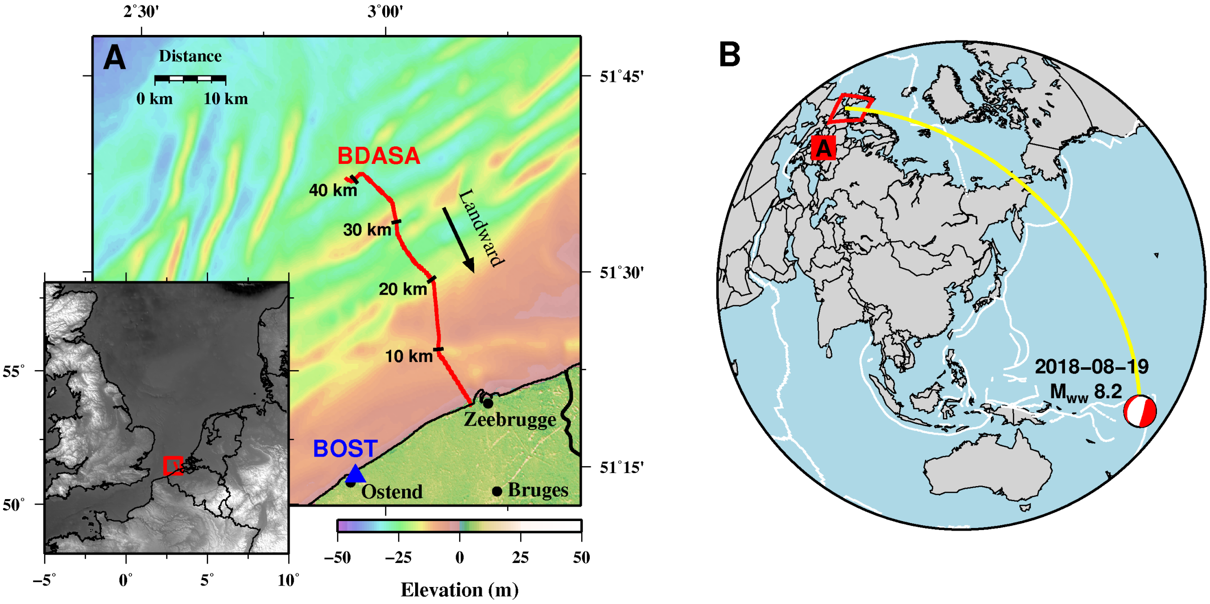

Figure 1: **Array location** (A) Local map showing the location Belgium Distributed Acoustic Sensing Array (BDASA, red line) and nearby broadband station BOST (blue triangle), with a regional map inset. (B) World map showing the location of the array (red box), the GCMT solution for the 2018-08-19 M8.2 Fiji deep earthquake, and great circle path between the earthquake epicenter and the array (yellow).

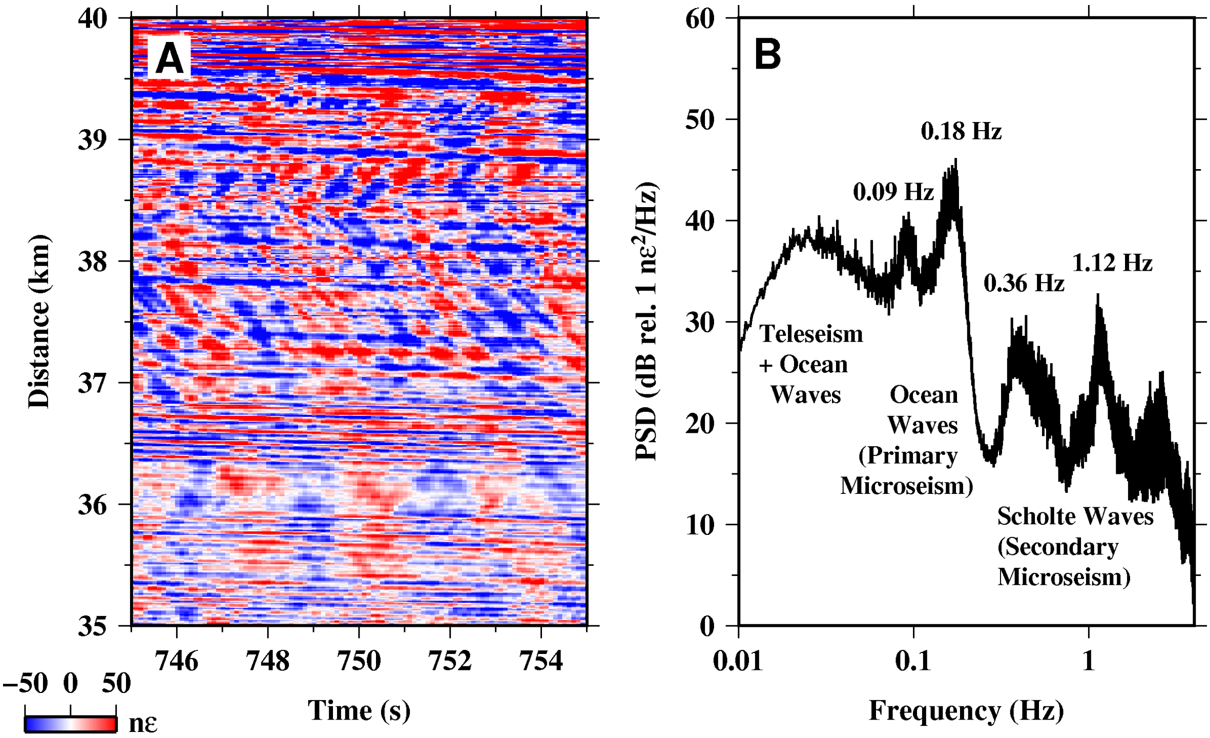

Figure 2: **Raw DAS data** (A) Ten seconds of raw distributed acoustic sensing (DAS) data along the last five kilometers of the array illustrating the superposition of coherent signals from ocean and seismic waves propagating both landward and seaward across the array. (B) Mean power spectral density (PSD) of raw DAS strain data over the complete 1 hr record between 35-40 km (same position as (A)).

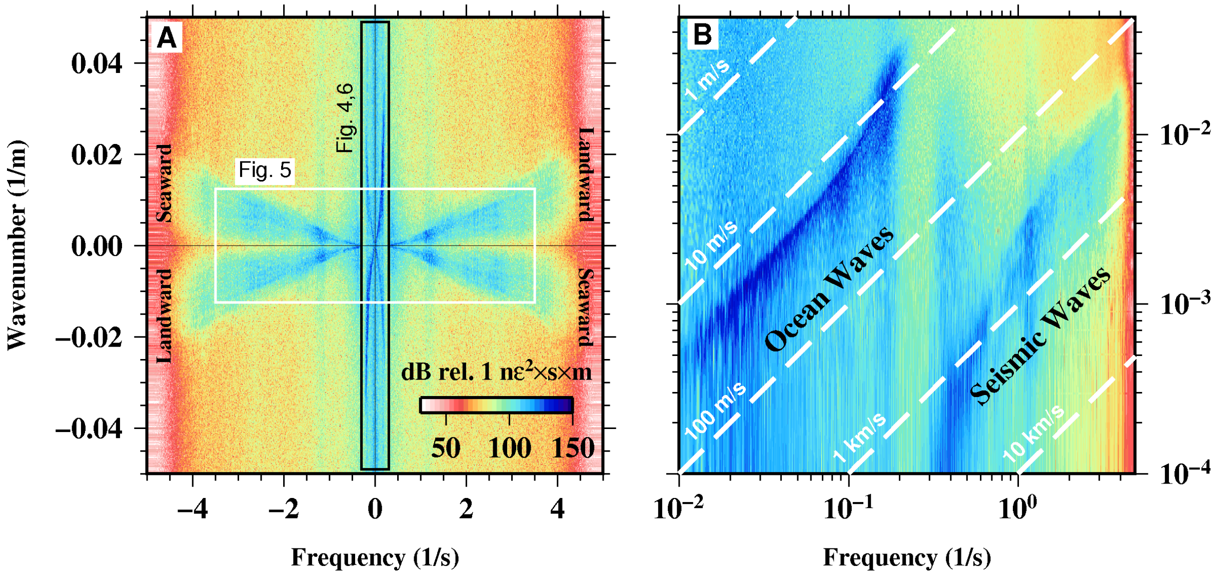

Figure 3: **Separation of ocean and seismic waves** (A) Raw frequency-wavenumber power spectrum of 1 hr of strain data across the full 42-km array. (B) Quadrant 1 (landward-propagating waves) plotted in logarithmic space, showing coherent ocean wave energy at low frequencies and coherent seismic wave energy at high frequencies. Dashed white lines are plotted along contours of constant phase velocity ($c = f/k$).

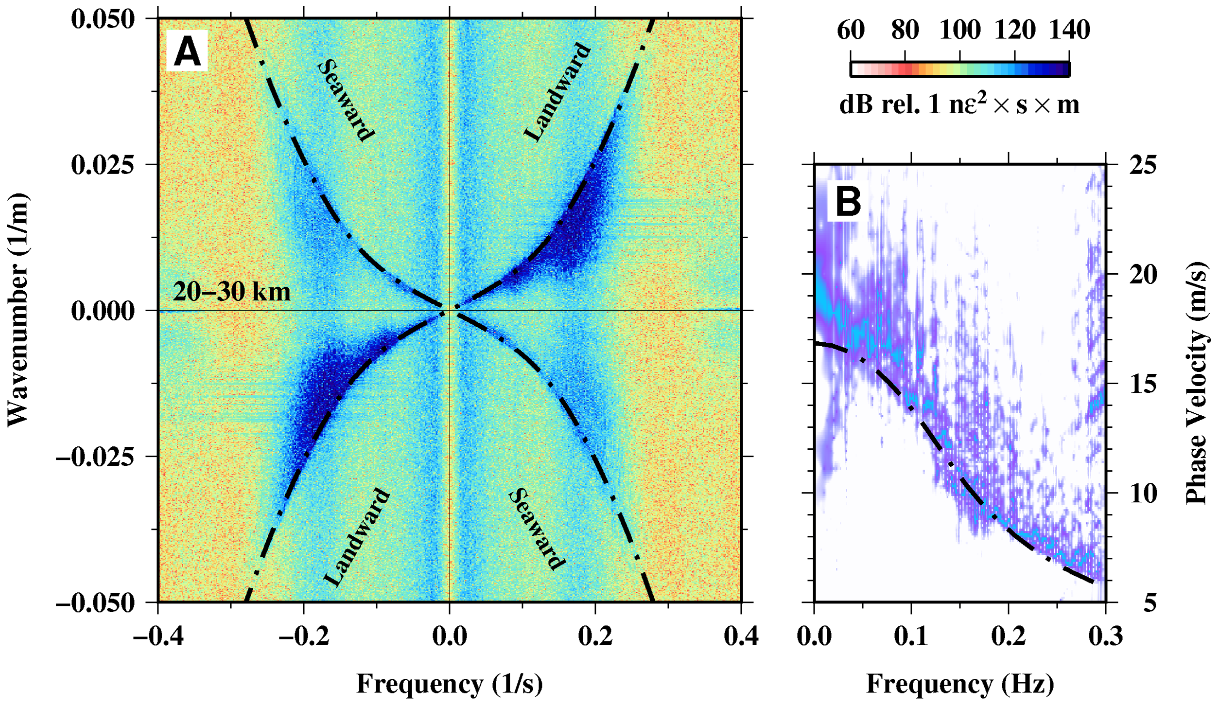

Figure 4: **Ocean surface gravity waves** (A) Raw distributed acoustic sensing frequency-wavenumber (f-k) spectrum calculated over 10 min between 20-30 km, showing strong landward-propagating and weak seaward-propagating ocean surface gravity waves. (B) The f-k spectrum from quadrant 1 of (A) projected into phase velocity space showing coherent dispersion from ~ 17 m/s at small wavenumbers to ~ 6 m/s at 0.3 Hz (each frequency bin is normalized). Both (A) and (B) are overlaid with the theoretical dispersion curve for ocean surface gravity waves, evaluated at a water depth of 25 m (black).

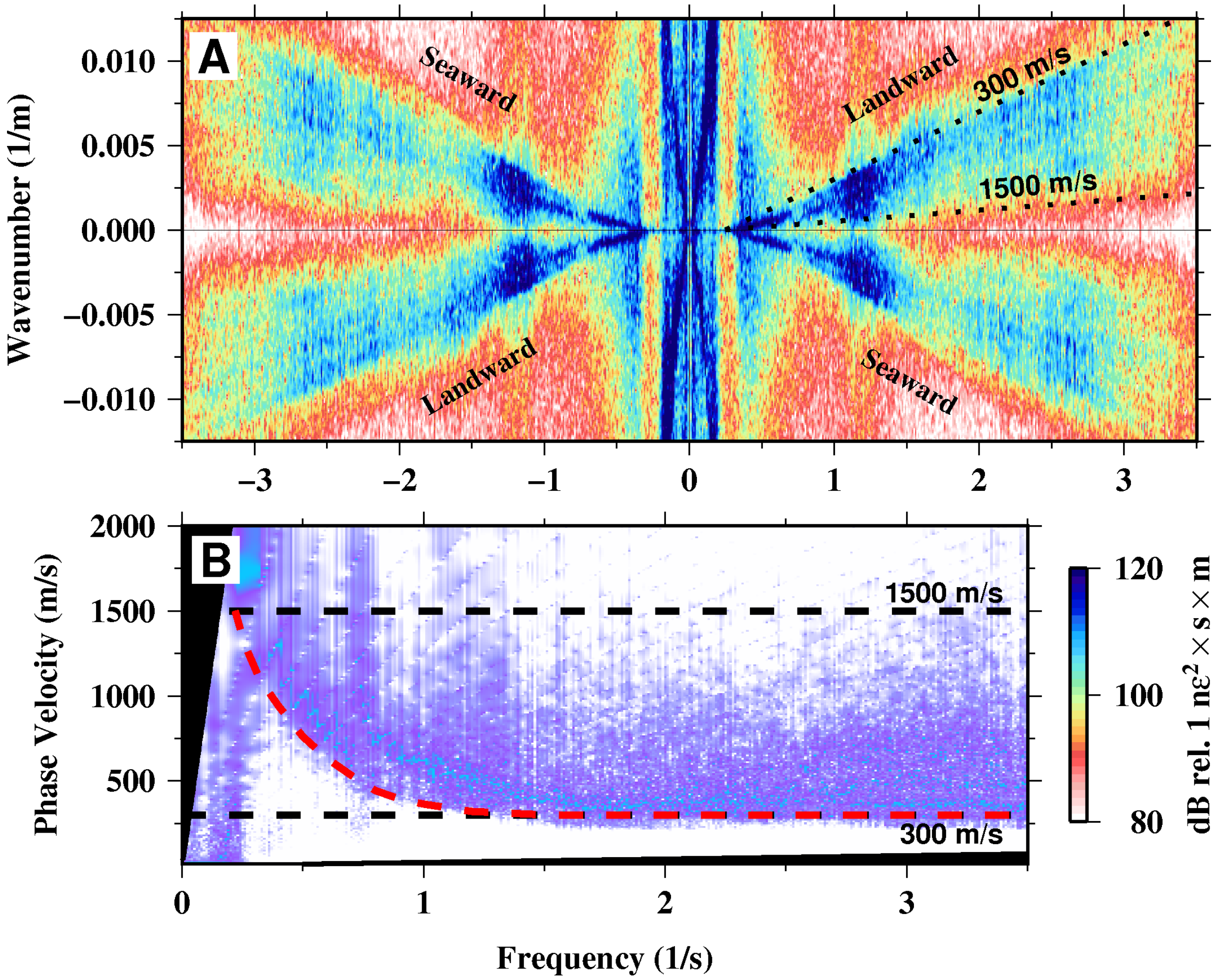

Figure 5: **Scholte (seismic) waves** (A) Raw distributed acoustic sensing frequency-wavenumber (f-k) spectrum calculated over 1 hr between 35-40 km, showing symmetric landward- and seaward-propagating Scholte waves between 0.3-3.5 Hz. (B) The f-k spectrum from quadrant 1 of (A) projected into phase velocity space showing coherent dispersion from $\sim$ 1500 m/s at 0.36 Hz to $\sim$ 300 m/s above 1 Hz (each frequency bin is normalized). Both (A) and (B) are overlaid with contours of constant velocity at 1500 and 300 m/s (black), and an approximate dispersion curve is hand-drawn in (B) (red).

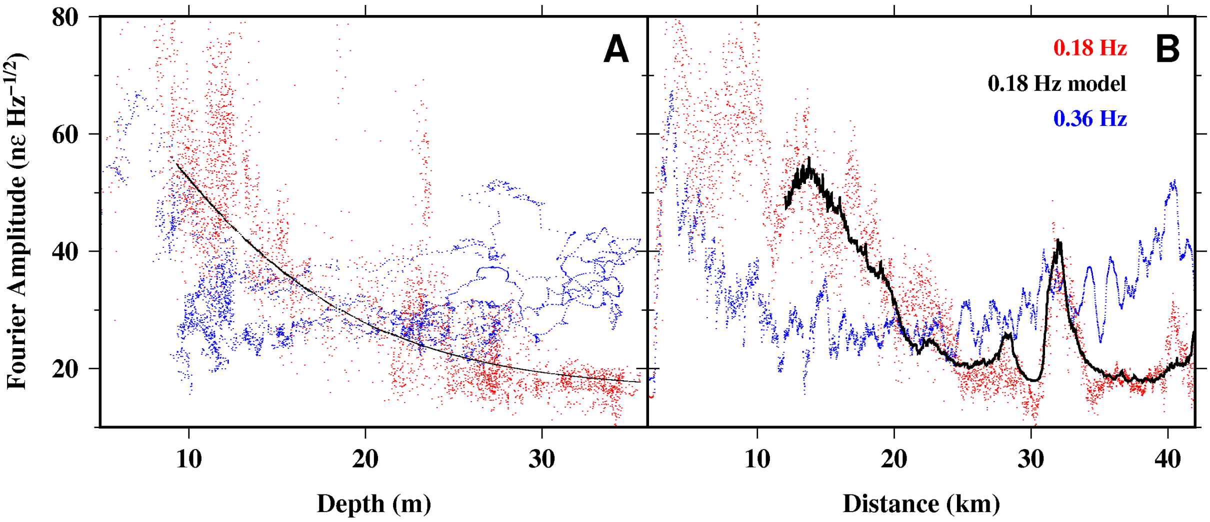

Figure 6: **Depth and distance scaling** (A) Fourier components of the raw distributed acoustic sensing strain spectrum at 0.18 (primary microseism, red) and 0.36 Hz (secondary microseism, blue) calculated at each channel plotted versus water depth. Also shown is the model of 0.18 Hz noise as a function of theoretical seafloor pressure described in the text (black). (B) Same as (A) but plotted with distance along the fiber.

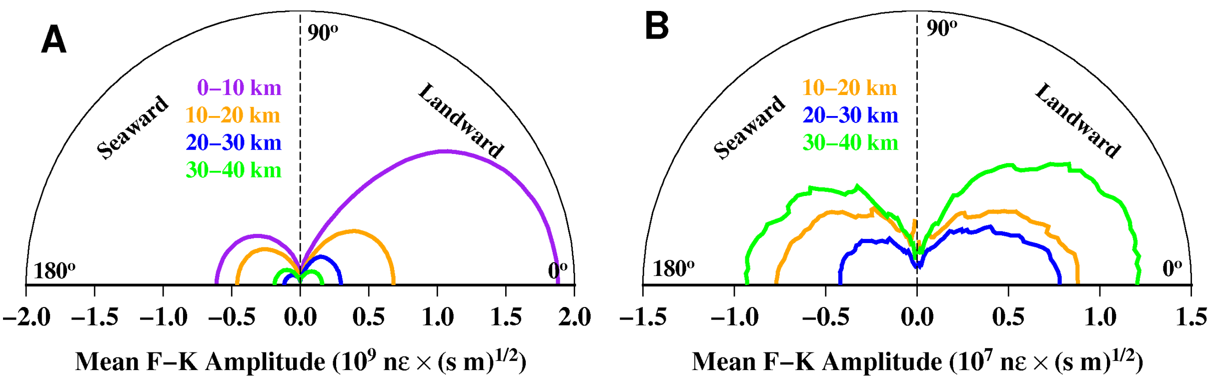

Figure 7: **Directional spectra** (A) Mean frequency-wavenumber (f-k) amplitude of ocean waves (primary microseism) as a function of azimuth calculated between 0.05-0.25 Hz using the ocean surface gravity wave dispersion relation for each of four 10-km array segments. (B) Mean f-k amplitude of Scholte waves (secondary microseism) as a function of azimuth calculated between 1.5-3.5 Hz assuming a true phase velocity of 300 m/s and no dispersion across this frequency band.

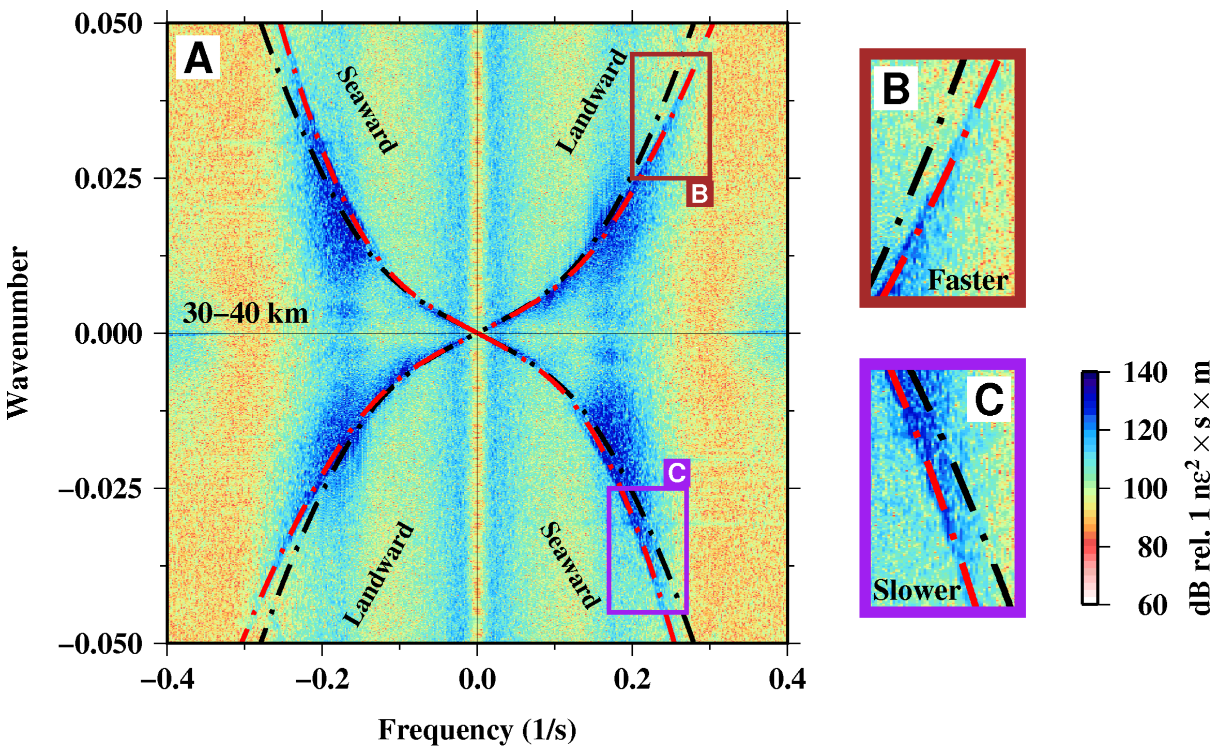

Figure 8: **Ocean currents** (A) Raw distributed acoustic sensing frequency-wavenumber spectrum calculated over 10 min between 30-40 km, showing asymmetrical dispersion due to an ocean current. (B),(C) Insets to (A) illustrating how landward-propagating ocean waves exhibit faster velocities than seaward-propagating ocean waves. The theoretical dispersion curves for ocean surface gravity waves are plotted with (red) and without (black) the effect of a mean-flow current.

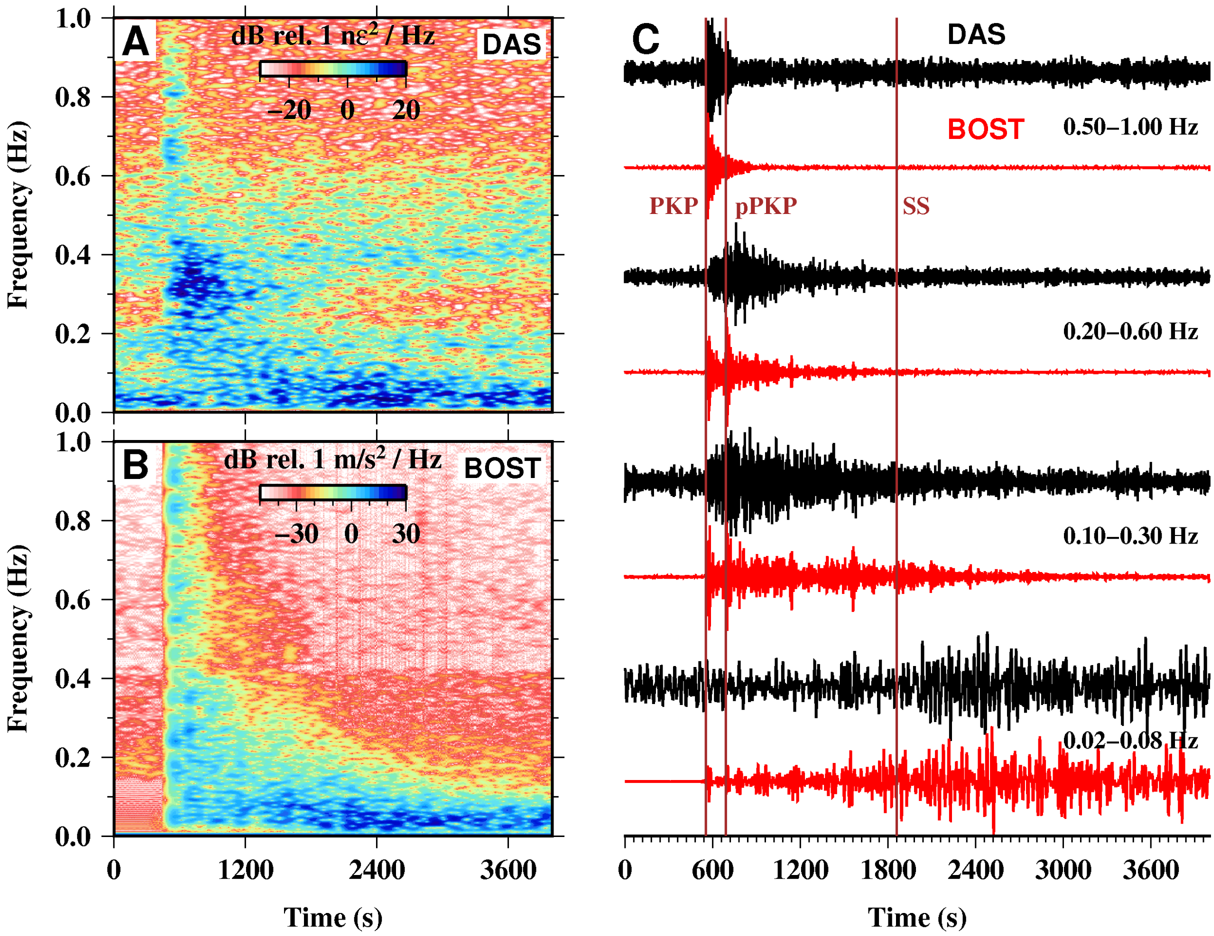

Figure 9: **Teleseismic waveforms** (A) Spectrogram of power spectral density (PSD) over time for the f-k filtered and stacked distributed acoustic sensing (DAS) beam trace (black in (C)), showing strong energy between 0-1 Hz around the arrival of the PKP phase around 550 s and below 0.1 Hz following the arrival of the SS phase around 1860 s. (B) Spectrogram for the rotated BOST channel (red in (C)), showing the same major features. (C) Stacked DAS beam trace (black) filtered to various bands between 0.02 and 1 Hz compared with amplitude-normalized particle velocity from broadband station BOST rotated into the mean azimuth of the DAS array (red).

References

1. Lay ed., T. *Seismological Grand Challenges in Understanding Earth's Dynamic Systems* in *Report to the National Science Foundation* (IRIS Consortium, 2009).

2. McGuire, J., Plank, T. & et al. *The SZ4D Initiative: Understanding the Processes that Underlie Subduction Zone Hazards in 4D* in *Vision Document Submitted to the National Science Foundation* (The Iris Consortium, 2017).

3. Suetsugu, D. & Shiobara, H. Broadband ocean-bottom seismology. *Annu. Rev. Earth Planet. Sci.* **42,** 27–43 (2014).

4. Forsyth, D., Webb, S., Dorman, L. & Shen, Y. Phase velocities of Rayleigh waves in the MELT experiment on the East Pacific Rise. *Science* **280,** 1235–1238 (1998).

5. Toomey, D., Wilcock, W., Solomon, S., Hammond, W. & Orcutt, J. Mantle seismic structure beneath the MELT region of the East Pacific Rise from P and S wave tomography. *Science* **280,** 1224–1227 (1998).

6. Webb, S., Deaton, T. & Lemire, J. A broadband ocean-bottom seismometer system based on a 1-Hz natural period geophone. *Bull. Seismol. Soc. Am.* **91,** 304–312 (2001).

7. Dolenc, D., Romanowicz, B., Stakes, D., McGill, P. & Neuhauser, D. Observations of infragravity waves at the Monterey ocean bottom broadband station (MOBB). *Geochemistry, Geophysics, Geosystems* **6** (2005).

8. Suetsugu, D. *et al.* Mantle discontinuity depths beneath the west Philippine basin from receiver function analysis of deep-sea borehole and seafloor broadband waveforms. *Bull. Seismol. Soc. Am.* **95,** 1947–1956 (2005).

9. Shinohara, M. *et al.* Aftershock observation of the 2011 off the Pacific coast of Tohoku Earthquake by using ocean bottom seismometer network. *Earth Planets Space* **63,** 835–840 (2011).

10. Ito, A. *et al.* Detection of small earthquakes along the Pacific-Antarctic Ridge from T-waves recorded by abyssal ocean-bottom observatories. *Mar. Geophys. Res.* **33,** 229–238 (2012).

11. Sugioka, H. *et al.* Tsunamogenic potential of the shallow subduction plate boundary inferred from slow seismic slip. *Nat. Geosci.* **5,** 414–418 (2012).

12. Tan, Y., Tolstoy, M., Waldhauser, F. & Wilcock, W. Dynamics of a sea-floor spreading episode at the East Pacific Rise. *Nature* **540,** 261–265 (2016).

13. Hello, Y., Oge, A., Sukhovich, A. & Nolet, G. Modern mermaids: New floats image the deep Earth. *Eos Trans. AGU* **92,** 337–338 (2011).

14. Frye, D. *et al. An acoustically-linked deep-ocean observatory* in *Oceans 2005–Europe, vol. 2* (Brest, France, 2005), 969–974.

15. Berger, J., Laske, G., Babcock, J. & Orcutt, J. An ocean bottom seismic observatory with near real-time telemetry. *Earth and Space Science* **3,** 66–77 (2016).

16. Goertz, A. & Wuestefeld, A. Real-time passive monitoring with a fibre-optic ocean bottom array. *First Break* **36,** 55–61 (2018).

17. Marra, G. *et al.* Ultrastable laser interferometry for earthquake detection with terrestrial and submarine cables. *Science* **361,** 486–490 (2018).

18. Mestayer, J. *et al. Field trials of distributed acoustic sensing for geophysical monitoring* in *SEG Technical Program Expanded Abstracts 2011* (2011), 4253–4257.

19. Mateeva, A. *et al. Advances in distributed acoustic sensing (DAS) for VSP* in *SEG Technical Program Expanded Abstracts 2012* (2012), 1–5.

20. Parker, T., Shatalin, S. & Farhadiroushan, M. Distributed Acoustic Sensing - A new tool for seismic applications. *First Break* **32,** 61–69 (2014).

21. Jousset, P., Reinsch, T., Henninges, J., Blanck, H. & Ryberg, T. *Crustal Exploration and Monitoring Seismic Events with a Fibre-optic Cable Deployed at the Ground Surface in Iceland* in *EAGE/DGG Workshop on Fibre Optic Technology in Geophysics* (Potsdam, Germany, 2017).

22. Martin, E., Biondi, B., Karrenbach, M. & Cole, S. *Continuous Subsurface Monitoring by Passive Seismic with Distributed Acoustic Sensors - The "Stanford Array" Experiment* in *79th EAGE Conference and Exhibition Extended Abstracts* (Paris, France, 2017).

23. Lindsey, N. *et al.* Fiber-optic network observations of earthquake wavefields. *Geophys. Res. Lett.* **44,** 11792–11799 (2017).

24. Jousset, P. *et al.* Dynamic strain determination using fiber-optic cables allows imaging of seismological and structural features. *Nat. Comm.* **9,** 2509 (2018).

25. Li, Z. & Zhan, Z. Pushing the limit of earthquake detection with distributed acoustic sensing and template matching: a case study at the Brady geothermal field. *Geophys. J. Int* **215,** 1583–1593 (2018).

26. Wang, H. *et al.* Ground motion response to an ML 4.3 earthquake using co-located distributed acoustic sensing and seismometer arrays. *Geophys. J. Int.* **213,** 2020–2036 (2018).

27. Ajo-Franklin, J. *et al.* Using Dark Fiber and Distributed Acoustic Sensing for Near-Surface Characterization and Broadband Seismic Event Detection. *Scientific Reports* **9,** 1328 (2019).

28. Yu, C., Zhan, Z., Lindsey, N., Ajo-Franklin, J. & Robertson, M. The potential of DAS in teleseismic studies: Insights from the Goldstone Experiment. *Geophys. Res. Lett.* **46** (2019).

29. Pastor-Graells, J., Martins, H. F., Garcia-Ruiz, A., Martin-Lopez, S. & Gonzalez-Herraez, M. Single-shot distributed temperature and strain tracking using direct detection phase-sensitive OTDR with chirped pulses. *Optics Express* **24,** 13121–13133 (2016).

30. Longuet-Higgins, M. A theory of the origin of microseisms. *Phil. Trans. Roy. Soc. A* **243,** 1–35 (1950).

31. Holthuijsen, L. *Waves in Oceanic and Coastal Waters* (Cambridge University Press, 2007).

32. Rauch, D. *Seismic interface waves in coastal waters: a review* in *SACLANTCEN Report SR 42* (1980).

33. Kedar, S. *et al.* The origin of deep ocean microseisms in the North Atlantic Ocean. *Proceedings of the Royal Society A* **464,** 777–793 (2008).

34. Haubrich, R. & McCamy, K. Microseisms: coastal and pelagic sources. *Reviews of Geophysics* **7,** 539–571 (1969).

35. Cessaro, R. Sources of primary and secondary microseisms. *Bull. Seis. Soc. Am.* **84,** 142–148 (1994).

36. Bromirski, P., Duennebier, F. & Stephen, R. Mid-ocean microseisms. *Geochemistry, Geophysics, Geosystems* **6** (2005).

37. Bromirski, P. Vibrations from the "Perfect Storm". *Geochemistry, Geophysics, Geosystems* **2** (2001).

38. Hasselmann, K. A statistical analysis of the generation of microseisms. *Reviews of Geophysics* **1,** 177–210 (1963).

39. Martin, E. *Passive imaging and characterization of the subsurface with distributed acoustic sensing* (Ph.D. Thesis, Dept. of Geophysics, Stanford University, Stanford, CA, 2018).

40. Chapron, B., Collard, F. & Ardhuin, F. Direct measurements of ocean surface velocity from space: Interpretation and validation. *J. Geophys. Res.: Oceans* **110,** C07008 (2005).

41. Paduan, J. & Washburn, L. High-frequency radar observations of ocean surface currents. *Ann. Rev. Marine Sci.* **5,** 115–136 (2013).

42. MODE Group. The Mid-Ocean Dynamics Experiment. *Deep Sea Research* **25,** 859–910 (1978).

43. Lumpkin, R. & Pezos, M. Measuring surface currents with Surface Velocity Program drifters: the instrument, its data, and some recent results. *Lagrangian analysis and prediction of coastal and ocean dynamics,* 39–67 (2007).

44. Wunsch, C. *Modern observational physical oceanography* (Princeton University Press, 2015).

45. Huang, N., Chen, D., Tung, C. & Smith, J. Interactions between steady non-uniform currents and gravity waves with applications for current measurements. *Journal of Physical Oceanography* **2,** 420–431 (1972).

46. Webb, S. & Crawford, W. Shallow-water broadband OBS seismology. *Bull. Seis. Soc. Am.* **100,** 1770–1778 (2010).

47. Williams, E., Zhan, Z., Karrenbach, M., Cole, S. & LaFlame, L. *Dense mapping of shallow velocity structure in the Raymond Basin using the Pasadena Distributed Acoustic Sensing Array* in *Southern California Earthquake Center Annual Meeting, Proceedings Vol. XXVIII* (Contribution No. 8543, Palm Springs, California, 2018).

48. Costa, L., Martins, H., Martin-Lopez, S., Fernández-Ruiz, M. & Gonzalez-Herraez, M. *Reaching pε/Hz sensitivity in a distributed optical fiber strain sensor* in *Optical Fiber Sensors Conference* (Lausanne, Switzerland, 2018), TuD3.

49. Kaplan, D., Largier, J., Navarrete, S., Guinez, R. & Castilla, J. Large diurnal temperature fluctuations in the nearshore water column. *Estuarine and Coastal Shelf Science* **57,** 385–398 (2003).

50. MacDonald, I., Bender, L., Vardaro, M., Bernard, B. & Brooks, J. Thermal and visual time-series at a seafloor gas hydrate deposit on the Gulf of Mexico slope. *Earth and Planet. Sci. Lett.* **233,** 45–59 (2005).

51. Webb, S. Broadband seismology and noise under the ocean. *Reviews of Geophysics* **36,** 105–142 (1998).

52. Rost, S. & Thomas, C. Array seismology: methods and applications. *Reviews of Geophysics* **40,** 2-1–2-27 (2002).

53. Nakata, N., Chang, J., Lawrence, J. & Boue, P. Body wave extraction and tomography at Long Beach, California, with ambient-noise interferometry. *J. Geophys. Res.: Solid Earth* **120,** 1159–1173 (2015).

54. Friedrich, A., Krueger, F. & Klinge, K. Ocean-generated microseismic noise located with the Gräfenberg array. *Journal of Seismology* **2** (1998).

55. Traer, J., Gerstoft, P., Brominski, P. & Shearer, P. Microseisms and hum from ocean surface gravity waves. *Journal of Geophysical Research: Solid Earth* **117** (2012).

56. Bradner, H., Doods, J. & Foulks, R. Investigation of microseism sources with ocean-bottom seismometers. *Geophysics* **30** (1965).

57. Goodman, D. *et al.* Directional spectra observations of seafloor microseisms from an ocean-bottom seismometer array. *Journal of the Acoustical Society of America* **86** (1989).

58. Dorman, L., Schreiner, A., Bibee, L. & Hildebrand, J. *Deep-water seafloor array observations of seismo-acoustic noise in the eastern Pacific and comparisons with wind and swell* in *Natural Physical Sources of Underwater Sound* (Springer, New York, 1993), 165–174.

59. Kibblewhite, A. & Wu, C. *A description of the ULF acoustic noise field in the ocean* in *Natural Physical Sources of Underwater Sound* (Springer, New York, 1993), 189–202.

60. Nye, T. & Yamamoto, T. Field Test of Buried Ocean-Wave Directional Spectrometer System. *Journal of Waterway, Port, Coastal, and Ocean Engineering* **120** (1994).

61. Hornman, K., Kuvshinov, B., Zwartjes, P. & Franzen, A. *Field trial of a broadside-sensitive distributed acoustic sensing cable for surface seismic* in *75th EAGE Conference and Exhibition Extended Abstracts* (London, U.K., 2013).

62. Mellors, R. *et al. Understanding distributed fiber optic sensing response for modeling of signals* in *SEG Technical Program Expanded Abstracts 2018* (2018), 4679–4682.

63. Lindsey, N., Rademacher, H., Dreger, D., Titov, A. & Ajo-Franklin, J. *How Broadband is DAS? Two Empirical Evaluations of Instrument Response* in *Seismological Society of America Annual Meeting 2019 Technical Sessions* (2019).

64. Fernandez-Ruiz, M. R., Martins, H. F., Pastor-Graells, J., Martin-Lopez, S. & Gonzalez-Herraez, M. Phase-sensitive OTDR probe pulse shapes robust against modulation-instability fading. *Optics Letters* **41,** 5756–5759 (2016).

65. Martins, H. F. *et al.* Distributed vibration sensing over 125 km with enhanced SNR using phi-OTDR over a URFL cavity. *Journal of Lightwave Technology* **33,** 2628–2632 (2015).

66. Pastor-Graells, J. *et al.* Chirped-pulse phase-sensitive reflectometer assisted by first-order Raman amplification. *Journal of Lightwave Technology* **35,** 4677–4683 (2017).

67. Kim, P. *et al.* Novel in-service supervisory system using OTDR for long-haul WDM transmission link including cascaded in-line EDFAs. *IEEE Photonics Technology Letters* **13,** 1136–1138 (2001).

68. Gyger, F., Rochat, E., Chin, S. & Thévenaz, L. Extending the sensing range of Brillouin optical time-domain analysis up to 325 km combining four optical repeaters. *Proceedings of SPIE,* 9157Q (2014).

69. Wang, Z. N. *et al.* Ultra-long phase-sensitive OTDR with hybrid distributed amplification. *Optics Letters* **39,** 5866–5868 (2014).

70. Fernandez-Ruiz, M. R., Martins, H. F., Costa, L., Martin-Lopez, S. & Gonzalez-Herraez, M. Steady-sensitivity distributed acoustic sensors. *Journal of Lightwave Technology* **36,** 5690–5696 (2018).

71. Goodman, J. *Introduction to Fourier Optics* (McGraw-Hill, 1994).

72. Fernandez-Ruiz, M. R. *et al.* Laser phase-noise cancellation in chirped-pulse distributed acoustic sensing. *Journal of Lightwave Technology* **36,** 979–985 (2018).

73. Gabai, H. & Avishay, E. On the sensitivyt of distributed acoustic sensing. *Opt. Lett.* **41,** 5648–5651 (2016).

74. Chen, D., Lui, Q. & He, Z. Phase-detection distributed fiber-optic vibration sensor without fading-noise based on time-gated digital OFDR. *Optics Express* **25,** 8315–8325 (2017).

Figure Legends

Figure 1: **Array location** (A) Local map showing the location Belgium Distributed Acoustic Sensing Array (BDASA, red line) and nearby broadband station BOST (blue triangle), with a regional map inset. (B) World map showing the location of the array (red box), the GCMT solution for the 2018-08-19 M8.2 Fiji deep earthquake, and great circle path between the earthquake epicenter and the array (yellow).

Figure 2: **Raw DAS data** (A) Ten seconds of raw distributed acoustic sensing (DAS) data along the last five kilometers of the array illustrating the superposition of coherent signals from ocean and seismic waves propagating both landward and seaward across the array. (B) Mean power spectral density (PSD) of raw DAS strain data over the complete 1 hr record between 35-40 km (same position as (A)).

Figure 3: **Separation of ocean and seismic waves** (A) Raw frequency-wavenumber power spectrum of 1 hr of strain data across the full 42-km array. (B) Quadrant 1 (landward-propagating waves) plotted in logarithmic space, showing coherent ocean wave energy at low frequencies and coherent seismic wave energy at high frequencies. Dashed white lines are plotted along contours of constant phase velocity ($c = f/k$).

Figure 4: **Ocean surface gravity waves** (A) Raw distributed acoustic sensing frequency-wavenumber (f-k) spectrum calculated over 10 min between 20-30 km, showing strong landward-propagating and weak seaward-propagating ocean surface gravity waves. (B) The f-k spectrum from quadrant 1 of (A) projected into phase velocity space showing coherent dispersion from $\sim$ 17 m/s at small wavenumbers to $\sim$ 6 m/s at 0.3 Hz (each frequency bin is normalized). Both (A) and (B) are overlaid with the theoretical dispersion curve for ocean surface gravity waves, evaluated at a water depth of 25 m (black).

Figure 5: **Scholte (seismic) waves** (A) Raw distributed acoustic sensing frequency-wavenumber (f-k) spectrum calculated over 1 hr between 35-40 km, showing symmetric landward- and seaward-propagating Scholte waves between 0.3-3.5 Hz. (B) The f-k spectrum from quadrant 1 of (A) projected into phase velocity space showing coherent dispersion from $\sim$ 1500 m/s at 0.36 Hz to $\sim$ 300 m/s above 1 Hz (each frequency bin is normalized). Both (A) and (B) are overlaid with contours of constant velocity at 1500 and 300 m/s (black), and an approximate dispersion curve is hand-drawn in (B) (red).

Figure 6: **Depth and distance scaling** (A) Fourier components of the raw distributed acoustic sensing strain spectrum at 0.18 (primary microseism, red) and 0.36 Hz (secondary microseism, blue) calculated at each channel plotted versus water depth. Also shown is the model of 0.18 Hz noise as a function of theoretical seafloor pressure described in the text (black). (B) Same as (A) but plotted with distance along the fiber.

Figure 7: **Directional spectra** (A) Mean frequency-wavenumber (f-k) amplitude of ocean waves (primary microseism) as a function of azimuth calculated between 0.05-0.25 Hz using the ocean surface

gravity wave dispersion relation for each of four 10-km array segments. (B) Mean f-k amplitude of Scholte waves (secondary microseism) as a function of azimuth calculated between 1.5-3.5 Hz assuming a true phase velocity of 300 m/s and no dispersion across this frequency band.

Figure 8: **Ocean currents** (A) Raw distributed acoustic sensing frequency-wavenumber spectrum calculated over 10 min between 30-40 km, showing asymmetrical dispersion due to an ocean current. (B),(C) Insets to (A) illustrating how landward-propagating ocean waves exhibit faster velocities than seaward-propagating ocean waves. The theoretical dispersion curves for ocean surface gravity waves are plotted with (red) and without (black) the effect of a mean-flow current.

Figure 9: **Teleseismic waveforms** (A) Spectrogram of power spectral density (PSD) over time for the f-k filtered and stacked distributed acoustic sensing (DAS) beam trace (black in (C)), showing strong energy between 0-1 Hz around the arrival of the PKP phase around 550 s and below 0.1 Hz following the arrival of the SS phase around 1860 s. (B) Spectrogram for the rotated BOST channel (red in (C)), showing the same major features. (C) Stacked DAS beam trace (black) filtered to various bands between 0.02 and 1 Hz compared with amplitude-normalized particle velocity from broadband station BOST rotated into the mean azimuth of the DAS array (red).

Supplementary Notes

Supplementary Note 1: Fiber-optic Cable

The BDASA occupied an optical fiber deployed within a power cable to the Belwind Offshore Wind Farm, offshore Belgium. The fiber is internally coupled with fillers to the cable's armor bedding (Supplementary Figure 1A). The cable consists of 3 core cables, an optical fiber, and a filler in polypropelene (PP) yarn. The outer serving in PP wraps the layer of round galvanized steel wires and is the layer that has direct contact with subsea sediments. Hence, vibrations that are passed from sediment into the fiber propagate through a frictional contact between adjacent components. The fiber and core cables are helically inserted into the cable.

Burial of the cable further attenuates vibrations generated by ocean gravity waves, as described in Godfrey, WO2018154275A1, 2018-02-09 [**patent**]. This is clearly shown in Figure S1B, where the strength of observed ocean wave energy in the 0.01-0.2 Hz band decreases as a function of increasing burial depth. Figure S1B plots channels at constant water depth, as the change in ocean-bottom pressure associated with increasing water depth is a much stronger signal across the array.

Increasing depth of burial also attenuates temperature variations from the ocean water above. However, temperature variations within the cable due to changing electric load can exceed 1 K. We do not analyze the effect of temperature in-situ.

Supplementary Note 2: 0.18 Hz Model

In order to fit depth-dependence of noise at the primary microseism peak (0.18 Hz), we first calculate a theoretical curve for the pressure at the seafloor under an ocean surface gravity wave as a function of seafloor depth. Here, we consider only p_d, the dynamic pressure due to wave propagation. The pressure profile with water depth for ocean surface gravity waves over a flat bed is given as

$$p_d(t,x) = \rho g \eta(t,x) \frac{\cosh(k(H+z))}{\cosh(kH)}$$

where ρg is the specific weight of water, $\eta(t,x)$ represents the sea-surface height along the propagating surface gravity wave, H is depth to the seafloor, and k is angular wavenumber [31]. Evaluated at the seafloor ($z = -H$), we find: $p_d(x) \propto \mathrm{sech}(k(x)\,H(x))$. In order to evaluate this expression, we solve the implicit dispersion relation for surface gravity waves ($\omega^2 = gk\tanh(kH)$) to find angular wavenumber $k = k(x)$ using an iterative scheme given the depth profile of the seabed $H(x)$ and frequency $\frac{\omega}{2\pi} = 0.18$ Hz. Finally, we perform a linear regression to find a single constant of proportionality between the Fourier amplitude at 0.18 Hz and our theoretical $p_d(x)$ as a function of depth/distance (i.e. $FFT_t\{\varepsilon\}(f = 0.18\mathrm{Hz}, x) = A\,p_d(x) + B$). The resulting pressure-depth model is plotted against BDASA data in Fig. 3. We only perform this fit further than 12 km from shore where water depth is > 10 m, as shoaling waves in shallow water do not adhere to linear wave theory. We neglect any effects of variable burial depth of the fiber.

Supplementary Note 3: Directional Spectra

The directional spectra plotted in Fig. 7 (polar diagrams) are calculated from the frequency-wavenumber spectrum of raw BDASA strain records. For each wave type, we first assume a dispersion relation $\omega = \omega(k)$ and then evaluate ω for a range of apparent wavenumbers $k_a = k/\cos(\theta)$, corresponding to waves propagating across the array from oblique azimuths. For ocean surface gravity waves (Fig. 7A), we use the relation $\omega^2 = gk\tanh(kH)$. For Scholte waves (Fig. 7B), we use only 1.5-3.5 Hz, where the observed f-k spectrum appears non-dispersive, and assume constant phase velocity ($\omega \propto k$). The mean f-k amplitude is then obtained for each incident azimuth θ by interpolating the f-k spectral amplitudes along each calculated dispersion curve and averaging them. To separate the incoming and outgoing energy, we perform this calculation independently for f-k quadrants 1 and 2. We plot only $0 - 180^o$ because quadrants 1 and 3 (similarly, 2 and 4) are symmetrical by nature of the 2D FFT, so we cannot distinguish the direction of energy propagating perpendicular to the array (whether SW-NE or NE-SW).

Supplementary Note 4: Teleseism Extraction by Filtering

The superposition of coherent signals from ocean waves, Scholte waves, and teleseism in BDASA data makes interpretation of raw strain records challenging (Fig. 2A). Because these signals also inhabit overlapping frequency bands, simple time-domain or time-frequency filtering is insufficient to isolate individual signals. Instead, we employ a frequency-wavenumber filtering approach that exploits the dense spatial sampling and wide aperture of the BDASA. We first apply a 2D Hamming (cosine-sum) taper $W_H[n,m]$ to the raw t-x domain strain data $\varepsilon(t,x)$ and then compute the 2D Fast Fourier Transform (FFT) to obtain the f-k spectrum $\hat{\varepsilon}(f,k)$.

$$W_H[n,m] = \left(\frac{25}{46} - \frac{21}{46}\cos\left(\frac{2\pi n}{N_t}\right)\right)\left(\frac{25}{46} - \frac{21}{46}\cos\left(\frac{2\pi m}{N_x}\right)\right)$$

$$\hat{\varepsilon}(f,k) = FFT_{2D}\{W_H\, \varepsilon(t,x)\}(f,k)$$

In the f-k domain, the spectrum is organized according to apparent phase velocity along the array. We only transform data from quasi-linear array segments because this simplifies interpretation of the f-k spectrum relative to a single reference direction (the axis of the fiber). Teleseismic phases from the Fiji deep earthquake, which is nearly antipodal to the BDASA, arrive with apparent horizontal velocity > 10 km/s, and for non-dispersive body waves the energy should appear in the f-k domain along a line of constant f/k. However, the aperture of the BDASA determines wavenumber domain sampling, relegating energy from teleseismic phases to the zero-wavenumber bin across most of the frequency range of interest. For example, a 5-km transformed segment with 500 channels at 10-m spacing has 0.0002 m^{-1}-wide wavenumber bins, and the wavenumber of a 1 Hz teleseismic P-wave arriving at apparent horizontal velocity $c = f/k \approx 10000$ m/s is ~ 0.0001 m^{-1}. The f-k domain also contains directional information: for the BDASA, energy that appears in f-k quadrants 1 and 3 corresponds to waves propagating land-ward (from the north/west) across the array, and energy that appears in quadrants 2 and 4 corresponds to waves propagating sea-ward (from the south/east). Hence, teleseismic phases from the Fiji earthquake only appear in f-k quadrants 1 and 3.

In conventional f-k processing, we would apply a dip filter to isolate a non-dispersive signal, which passes a sector between two lines of constant f/k. However, we found that this approach is not numerically stable for low frequencies where the pass sector is only a few bins wide. Consequently we reverted to a simple approach, using a 2D rectangular bandpass filter between 0.001-1 Hz and 0-0.002 m^{-1}, without any tapering (Supplementary Figure 2). We apply this filter only in f-k quadrants 1 and 3 to attenuate all energy propagating across the BDASA from the south/east. With $f_1 = 0.001\text{Hz}$, $f_2 = 1\text{Hz}$, $k_1 = 0\text{m}^{-1}$, $k_2 = 0.002\text{m}^{-1}$, $f_m = (f_1 + f_2)/2$, and $k_m = (k_1 + k_2)/2$, the filter $H(f, k)$ can be expressed as:

$$H(f,k) = \Pi\left(\frac{f - f_m}{f_2 - f_1}\right)\Pi\left(\frac{k - k_m}{k_2 - k_1}\right) + \Pi\left(\frac{f + f_m}{f_2 - f_1}\right)\Pi\left(\frac{k + k_m}{k_2 - k_1}\right)$$

where Π denotes a rectangular boxcar of unit amplitude. This filter is non-causal ($h(t, x) = FFT_{2D}^{-1}\{H(f, k)\}$ is even) and exhibits some Gibbs ringing because of its finite implementation, so a more careful approach may need to be considered for accurate seismic travel-time picking in future studies. After filtering, some residual energy from Scholte waves remains, so we stack across a 5-km segment to improve SNR and isolate teleseismic body waves. When the stack is applied across many sub-sections of the array, relatively high spatial coherence is observed for both P- and S-wave phases (Supplementary Figure 5).

Supplementary Note 5: Teleseism Waveform Fidelity

As discussed in the main text, recovered P-waves exhibit low-to-moderate waveform fidelity at high frequencies and recovered S-waves exhibit moderate-to-high waveform fidelity at low frequencies. Fig. S3A shows the evolution of P waveforms along the array, showing that some coherent energy arrives before the first arrival because of our acausal filter. Overall, P-wave fidelity is low, with a maximum correlation coefficient of 0.26 in the 0.5-1 Hz frequency band calculated in a window centered between the PKP and pPKP arrivals (Supplementary Figure 3). However, a high spike in correlation coefficient up to 0.39 is observed when the first PKP motions enter the correlation window (Supplementary Figure 3B), suggesting that the BDASA beam trace contains sufficient phase information at high frequencies to permit correlation-based detection algorithms such as template matching. Overall, S-wave fidelity is moderate to high, with a maximum correlation coefficient of 0.60 in a window centered around the SS phase, and average correlation coefficient greater than 0.40 throughout the complete S-wave train (Supplementary Figure 4).

Supplementary Note 6: Teleseism Amplitude Comparison

The 2018-08-19 $M_w 8.2$ Fiji deep earthquake is an atypical event to consider when testing the seismic monitoring capabilities of an instrument, so we include some comparative analysis here. With an epicentral depth around 600 km, the Fiji earthquake did not produce a significant surface wave train. The BDASA was also recording at an epicentral distance of 146^o, in the "shadow zone," meaning that the primary body phases observed were PKP and SS, the former of which can be strongly attenuated. Comparing the velocity spectrum of the Fiji earthquake recorded at BOST with mean velocity spectra of regional and teleseismic earthquakes [**clinton:2002**], we observe an expected correspondence between the Fiji event and mean $M8.0$ event over a broad band, with stronger S-wave energy at low frequencies than in the mean $M8.0$ event (Supplementary Figure 6). Because we have recovered the principal phases of the Fiji earthquake between 0.01-1 Hz on the BDASA, even in a high-noise shallow-water environment, we can assume that the spectrum observed on nearby broadband BOST exceeds the instrumental noise floor of the BDASA across this band. Hence, we can compare the mean spectra of other event sizes and distances from clinton:2002 indirectly with our demonstrated detection capabilities. As shown in Supplementary Figure 6, the Fiji earthquake observed at BOST and BDASA is a relatively weak signal, with regional earthquakes ($\sim$ 100 km epicentral distance) above $M3.5$ exceeding this threshold across most of their band.

738 # Supplementary Figures

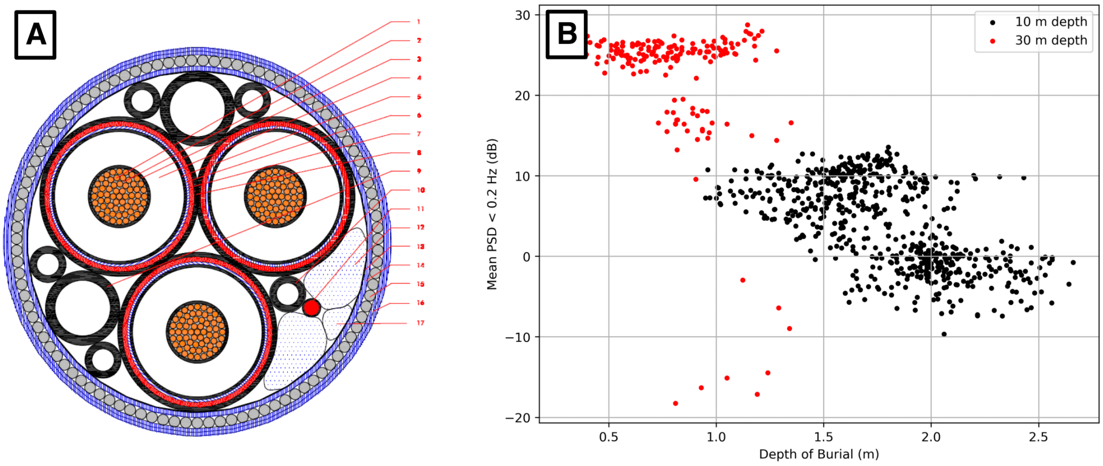

Figure 10: **Supplementary Figure 1: Cable coupling** (A) Schematic cable cross-section. Number 11 (red) indicates the position of the fiber. (B) Scaling of observed ocean wave energy with depth of burial for each of two water depths (10 m in black, 30 m in red).

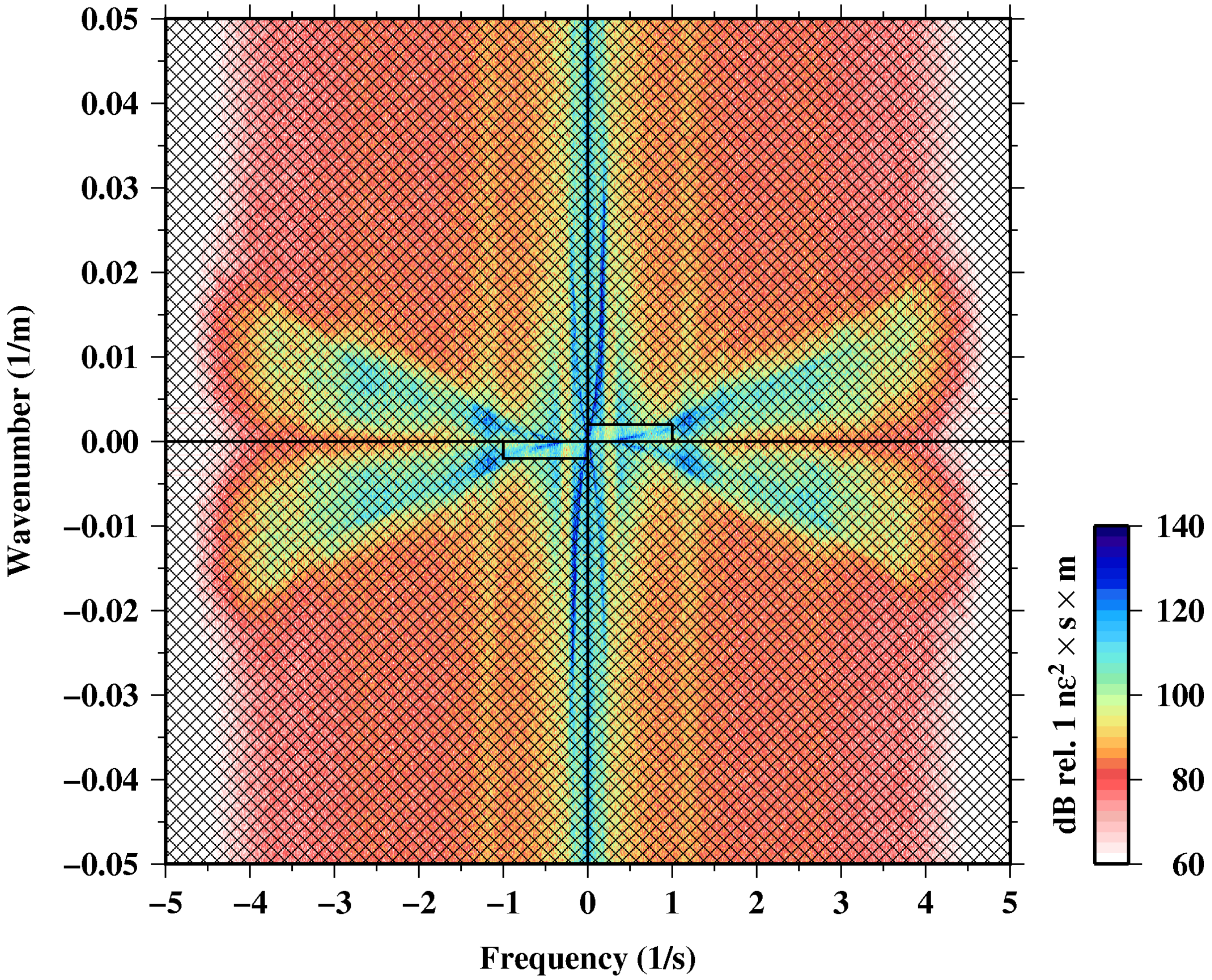

Figure 11: **Supplementary Figure 2: Frequency-wavenumber filter** The rectangular frequency-wavenumber filter applied to preserve only seismic waves in quadrants 1 and 3, indicating propagation from the north/west. Shaded regions are zero, unshaded regions are 1. The inverse 2D Fast Fourier Transform was computed, time-series from each channel between 35 and 40 km were stacked, and finally a bandpass filter was applied to produce the waveforms shown in Fig. 9, Supp. Fig. 3, and Supp. Fig. 4.

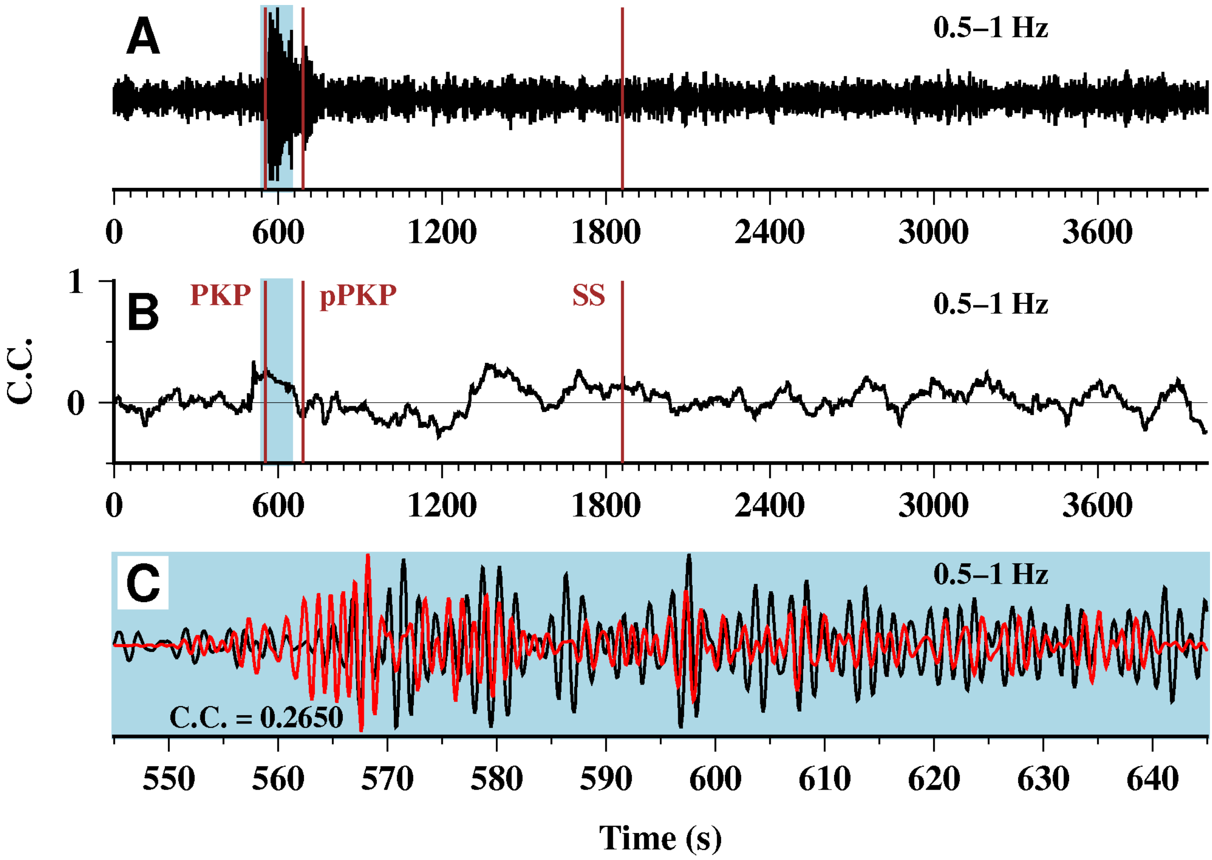

Figure 12: **Supplementary Figure 3: P-wave fidelity** (A) BDASA beam trace filtered 0.5-1 Hz (same as shown in Fig. 9c). (B) Correlation coefficient (C.C.) between the DAS and BOST waveforms filtered 0.5-1 Hz calculated over a 120 s moving window. (C) Blow-up of 1860-2320 s for the waveforms filtered 0.5-1 Hz around the arrival of the PKP phase just after 550 s, showing low-to-moderate waveform coherence between BOST (red) and BDASA (black) (C.C. = 0.2650). The time-shift between BOST and BDASA ($\sim$ 50 km apart) has not been removed.

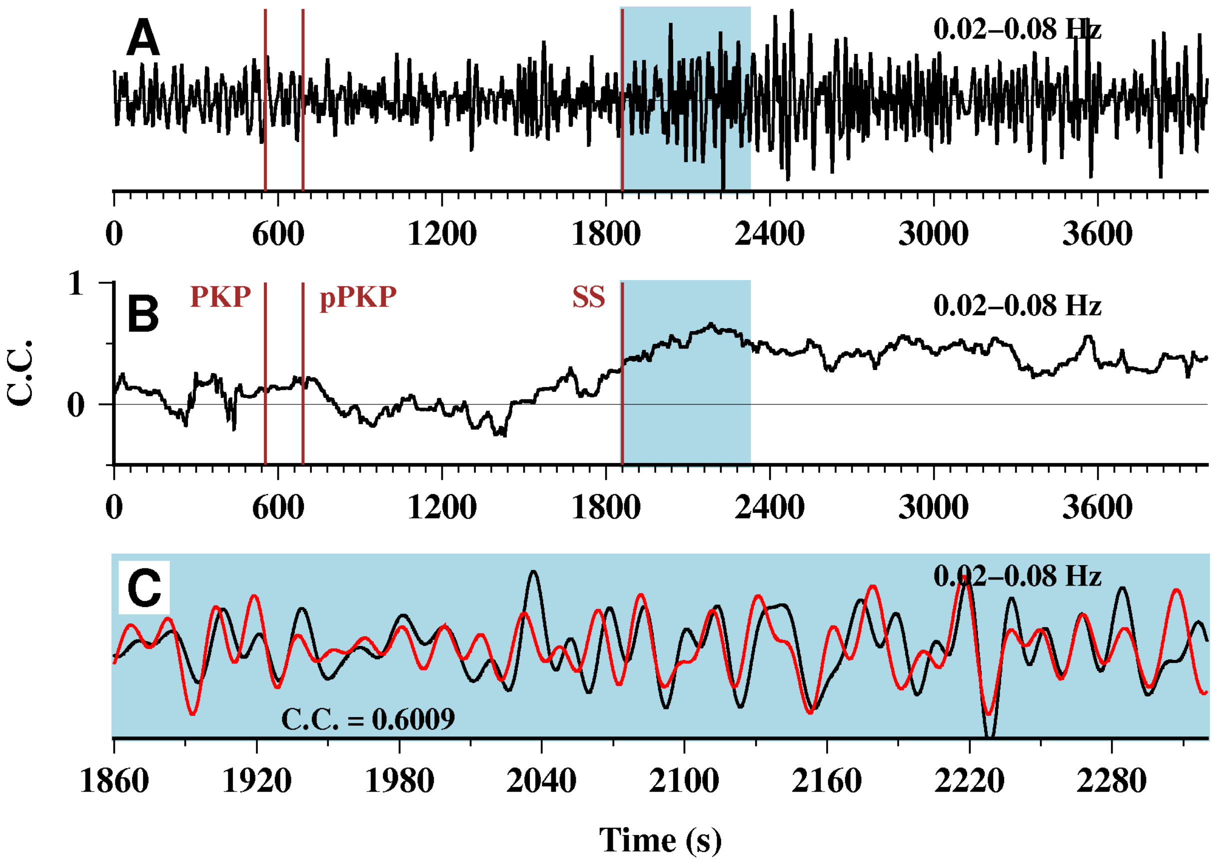

Figure 13: **Supplementary Figure 4: S-wave fidelity** (A) BDASA beam trace filtered 0.02-0.08 Hz (same as shown in Fig. 9c). (B) Correlation coefficient (C.C.) between the DAS and BOST waveforms filtered 0.02-0.08 Hz calculated over a 240 s moving window. (C) Blow-up of 1860-2320 s for the waveforms filtered 0.02-0.08 Hz around the arrival of the SS phase just after 1860 s, showing moderate-to-high waveform coherence between BOST (red) and BDASA (black) (C.C. = 0.6009).

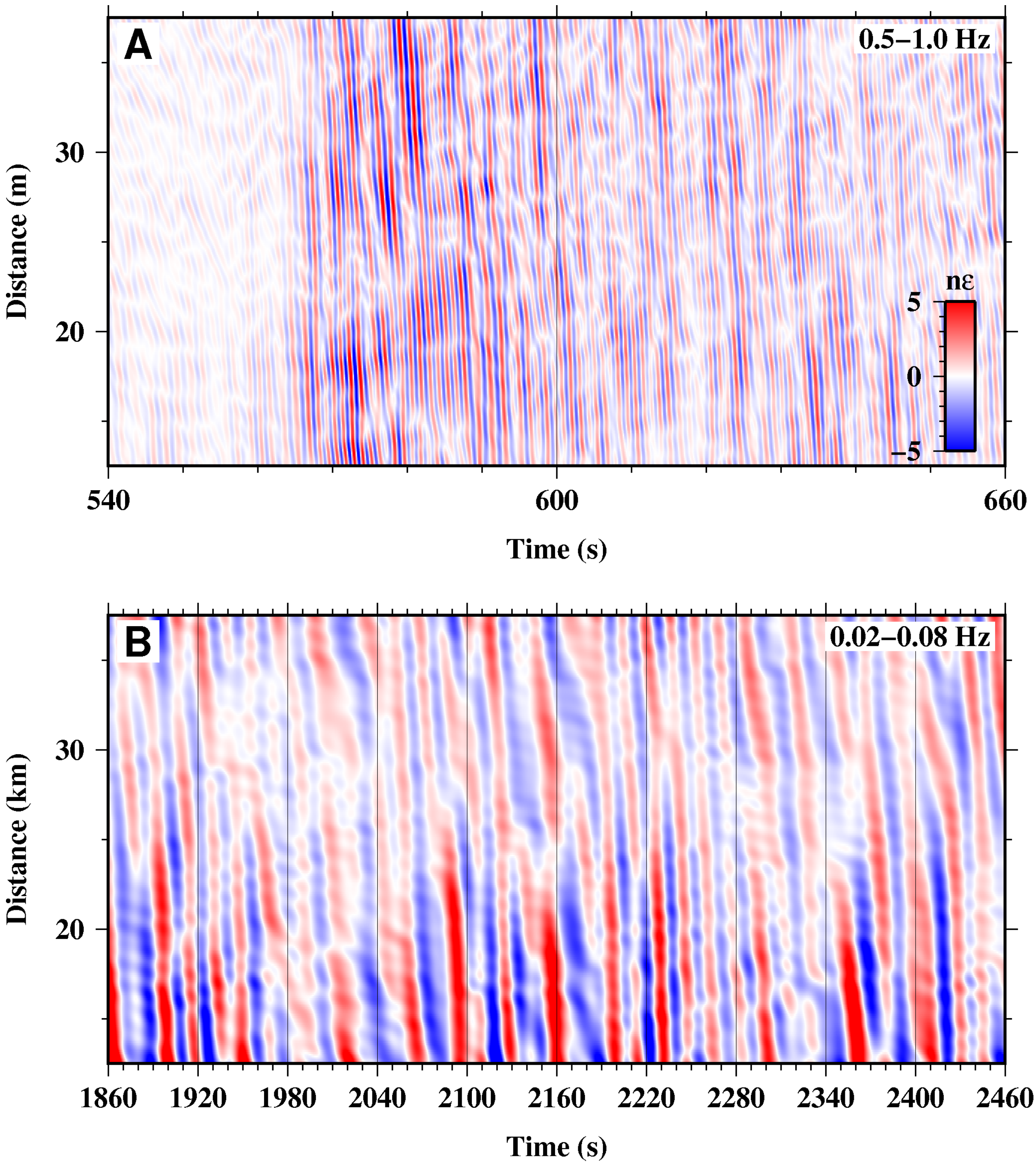

Figure 14: **Supplementary Figure 5: Waveform coherence** F-k filtered waveforms as shown in Figure 9 stacked in a 5-km moving window between 10 and 40 km (plotted at the midpoint of the stacked interval). (A) Bandpassed 0.5-1 Hz, showing the arrival of the PKP and pPKP phases, and (B) bandpassed 0.02-0.08 Hz, showing the arrival of the S-wave train. Note that the filtering procedure applied is non-causal, so some coherent PKP energy can be observed before the true PKP arrival, especially between 12-20 km. A similarly effective causal filter could be designed for more accurate travel-time picking.

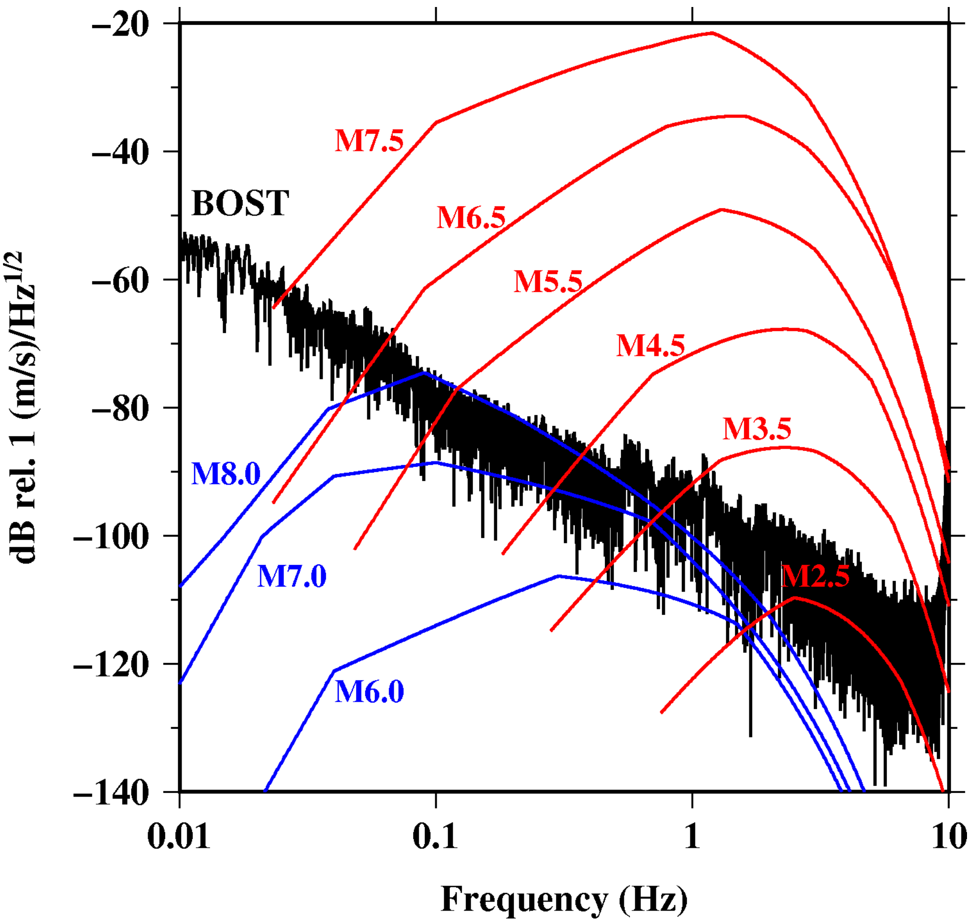

Figure 15: **Supplementary Figure 6: Earthquake scaling** BOST.BHE spectrum of the 2018-08-19 $M8.2$ Fiji deep earthquake (black) compared with average spectra of teleseismic (blue, ∼ 3000 km) and regional (red, ∼ 100 km) earthquakes from [**clinton:2002**] (converted from acceleration into velocity units).